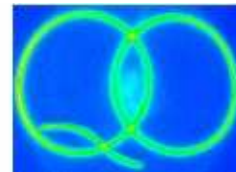# Optical Studies of Nano-Hole Arrays

Quantum Optics &
Quantum Information

Daniël Stolwijk
Report Master Project
July 18, 2008

Contents

1 Introduction

The success of micro- and nano-electronics is based on the precise control of electronics in a wide range of materials. At the heart of these electronic devices are semiconductors such as silicon, having the crucial property of an electronic band gap - a range of frequencies where electrons are forbidden from propagating. In the last couple of decades a lot of research in the field of photonics has been done in order to find materials that have a photonic band gap, here a range of frequencies of photons are forbidden from propagating by the material.

By now many of these structures, so-called photonic crystals, are known, produced and used in different applications. An example of a simple application of a photonic crystal is a high-efficiency light-emitting diode (LED) [1]. In standard LED's the efficiency is rather poor (3-20%) because the light emitted from the source travels in all directions and therefore only a fraction of the light generated, can actually leave the LED. However, if the source of the light would be surrounded by a photonic crystal, having a band gap at the relevant frequency, light would simply not be emitted in the directions where the crystal is, because there is no state available for the light. It is quantum-mechanically prohibited. Consequently, light can only escape in the right direction. In principle the efficiency of a LED could in this way be increased up to the internal efficiency - the efficiency with which the light is produced - which is about 90% [1]. Examples of other applications are high-capacity optical fibers, color pigments and photonic integrated circuits that manipulate light in addition to, or perhaps ultimately instead of, electric currents [2].

Most photonic crystals are made of dielectric materials. This is because metals are highly absorbing at optical frequencies. However, interesting phenomena take place when light is incident on a periodic metal structure, for instance giving rise to extraordinary high transmission through an optically thick gold layer perforated with a regular array of holes [3]. It is widely accepted that this effect is due to excitation of surface plasmons, electro-magnetic waves bound to the surface of a metal and a dielectric. It provides us with another way of controlling light, opening a range of new possibilities for applications. The detection efficiencies of certain types of photodetectors can for example be increased by an order of magnitude by making use of such a metal structures [1].

Currently, a lot of the physics that takes place when light interacts with periodic structures, both metal and dielectric ones, is not well-understood yet. To fully exploit the special properties of these photonic materials, a better understanding is required. In this report results are presented that provide new insight in the physics that takes place. In the first part of this report we investigate different types of metal structures, for instance how (nano-)antennas (or nano-pillars) that are placed on the structure, change the optical characteristics. We also examine the influence of the dielectric environment on the optical transmission through these optically thick structures. The second part of this report presents results of optical studies of a dielectric photonic crystal. Most quantitative descriptions in literature are based on rigorously solving Maxwell's equations [4, 5]. We apply and extend a simple theoretical model to describe observed resonant phenomena quantitatively.

The results of this research are published in references [6], [7] and [8]. These papers are attached in the appendix for completeness.

2 Theory

This report deals with the optical reflection and transmission of periodic nanostructures. The structures consist of a regularly perforated, 2-dimensional array. The lattice constant of these structures is comparable to the wavelength of the incident light, the size of the holes can be much smaller. As explained in the introduction, two types of arrays can generally be distinguished: metal and dielectric ones. Although quantitatively the interaction between light and the two types of arrays is quite different, reflection and transmission spectra show remarkable qualitative similarities. Sections 2.1 and 2.2 describe the different processes that contribute to the optical transmission and reflection of a metal and a dielectric nano-hole array, respectively. Section 2.3 discusses the general concept that is at the bottom of the observed similarities in the spectra.

2.1 Metal Nano-Hole Arrays

In this paragraph the processes that take place when light is incident on a metal nano-hole array (MNHA) are described. Also, a simple model that predicts where resonances in the optical transmission are to be expected, is presented.

The paths that light incident on a MNHA can take, are schematically shown in figure 1(a). In fact, three paths that contribute to the transmission, T, of light through a MNHA, can be distinguished. The first one is the light directly transmitted through the metal film and is given by [9]:

$$T(t, \lambda) = \exp(-4\pi\kappa t/\lambda), \tag{2.1}$$

with κ the extinction coefficient, t the thickness of the metal layer, and λ the wavelength of the incident light. For an optically thick MNHA, this contribution will turn out to be negligible (this will be justified in section 4.1).

The second contribution consists of the light transmitted through the subwavelength holes. It can be calculated by approximating the holes as independently radiating dipoles in a perfectly conducting, infinitely thin metal sheet. The contribution from this process to the transmission is given by [10]:

$$T(d, \lambda) = \frac{16\pi^3 d^6}{27a^2\lambda^4}, \tag{2.2}$$

with a the lattice constant and d the diameter of the holes. In practice the transmission due to this contribution will be lower, since real MNHA's are not ideal conductors, nor infinitely thin. For an optically thick MNHA, especially the latter reason will lower the contribution to the transmission.

The third contribution to the transmission is due to the periodicity of the array. A qualitative description of what takes place is as follows. The periodicity enables diffraction of the incident light. Evanescent electro-magnetic (EM) waves bound to the metal surface, called surface plasmon polaritons (SPPs), are excited [11]. The excited SPPs can tunnel to the other side of the array and can be transmitted as light [12]. Because of the diffraction from the lattice, only light with a well-defined wavelength

4
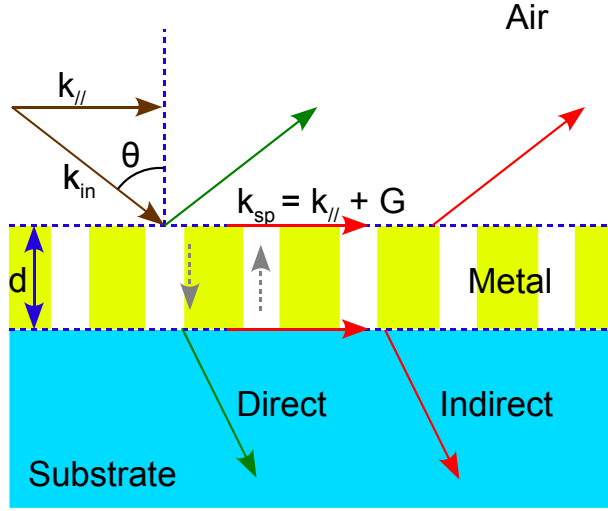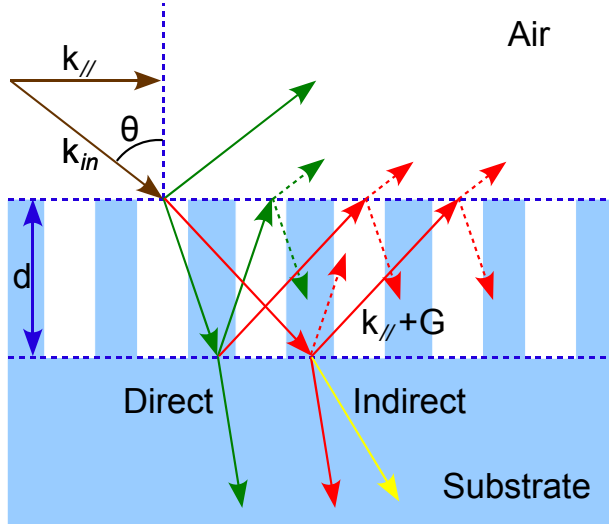
Figure 1: Panel (a) shows the different paths light can travel in a MNHA, panel (b) in a DNHA. In both panels the brown arrows refer to the incident light, the green arrows to the direct path and the red arrows to the indirect, resonant path. For the MNHA the direct path corresponds to the transmission directly through the holes, for the DNHA to the multilayer character of the system (indicated by multiple reflections at the surfaces). In both panels the indirect, resonant contribution is due to coupling to the lattice. At the MNHA, light couples to SPPs, at the DNHA the regularly perforated layer behaves as a leaky waveguide. For the DNHA the yellow arrow indicates the leak into the substrate side, where, contrary to the air side, also diffracted light can escape.

can excite a SPP. Therefore this contribution has a resonant character. We will refer to this contribution as the indirect contribution. The spectral position of these resonances can be quantified with a simple model [3]. The SPP dispersion relation for a smooth interface is given by [13]:

$$k_{\text{SPP}} = n_{\text{eff}} \frac{\omega_{\text{SPP}}}{c}, \tag{2.3}$$

with k_{SPP} the (complex) momentum of the SPP, and ω_{SPP} the (real) frequency. The effective index of refraction n_{eff}, is given by:

$$n_{\text{eff}} = \sqrt{\frac{\varepsilon_{\text{m}} \varepsilon_{\text{d}}}{\varepsilon_{\text{m}} + \varepsilon_{\text{d}}}}, \tag{2.4}$$

where ε_{m} and ε_{d} are the dielectric constants of the metal and the dielectric respectively. The momentum of the incident light alone is too small to directly to excite SPPs. The momentum necessary for this excitation is supplied by diffraction of the regular array of holes. This diffraction condition is expressed as:

$$\mathbf{k}_{\text{SPP}} = \mathbf{k}_{//} + \mathbf{G}, \tag{2.5}$$

where $\mathbf{k}_{//}$ is the parallel component of the incident light (the component of the incident light projected on the lattice, as in figure 1) and $\mathbf{G}$ the reciprocal lattice vector. This equation reveals the discrete character of the indirect contribution: for a 2-D lattice each integer linear combination of reciprocal lattice vectors corresponds to a resonance.

It should be emphasized that the contribution in the transmission consists of a non-resonant, direct process, as can be seen from equation 2.2 and a quantized, indirect process, as is revealed by equation 2.5.

2.2 Dielectric Nano-Hole Arrays

In a dielectric nano-hole array (DNHA) there are no free electrons and therefore no SPPs. However, as for the MNHA, light can again travel according several paths, as is schematically illustrated in figure 1(b). Again two physical processes contribute to the optical transmission: a direct and an indirect process. To calculate the direct contribution in the transmission, the DNHA can be treated as a homogeneous dielectric film with an effective refractive index. The film is surrounded by air at the top side and a substrate layer at the bottom side. Once the effective index is known, it is straightforward to calculate the reflection and transmission coefficients of this system for s- and p-polarized incident light (see section 5.2). The reflection and transmission coefficients have a non-resonant character as function of wavelength of the incident light.

The contribution of the indirect process arises from the coupling of light to a single leaky waveguide mode of the DNHA. The momentum necessary for the incident light, with wavevector $\mathbf{k}$, to couple to a guided mode, is supplied via diffraction at the lattice. This corresponds to adding a reciprocal lattice vector $\mathbf{G}$ of the crystal to the parallel component of the incident wavevector, $\mathbf{k}_{//}$:

$$\mathbf{k}_{\text{mode}} = \mathbf{k}_{//} + \mathbf{G}, \tag{2.6}$$
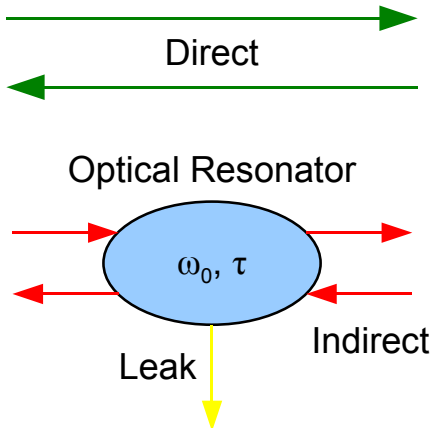
Figure 2: The optical resonator with a loss channel shown schematically. It describes the interference between a non-resonant direct channel and a resonant indirect one. The resonant channel has a resonant frequency, ω_0, and a lifetime, τ. For both an MNHA and a DNHA coupling to a resonant frequency occurs due to diffraction at the lattice as described by equation 2.7.

where $\mathbf{k}_{\mathrm{mode}}$ is determined by the dispersion relation (or band structure) of the photonic material that can accurately be calculated numerically [14]. This equation reveals the quantized, or mode-like structure of the indirect contribution in the optical transmission. The perforated layer thus behaves as a leaky waveguide for certain modes. Each mode can only leave the waveguide at the air interface by again giving up its gained momentum $\mathbf{G}$. The photon will be re-emitted with momentum $\mathbf{k}$. The situation is different at the substrate interface. As long as the refractive index of the substrate is higher than the effective refractive index of the perforated layer, photons can also leave the waveguide without giving up their gained momentum.

It should be stressed that the optical transmission consists of two contributions: a non-resonant, direct contribution, arising from the multi-layer character of the system and a mode-like, indirect contribution, stemming from the waveguide character (equation 2.6) of the system.

2.3 Fano Resonances

The previous two paragraphs show that the models used to describe the interaction between light and MNHAs on the one hand and light and DNHAs on the other hand, are related to different processes. However, as emphasized at the end of both sections and as indicated in figure 1, the processes contributing to the optical transmission show strong qualitative similarities: for both MNHAs and DNHAs there is a continuous, direct contribution and a mode-like, indirect one. The coupling to a resonant frequency occurs due to diffraction at the periodic structure and is in fact imposed by the same condition:

$$\mathbf{k}_{\mathrm{res}} = \mathbf{k}_{//} + \mathbf{G}, \tag{2.7}$$

where $\mathbf{k}_{\mathrm{res}}$ equals $\mathbf{k}_{\mathrm{SPP}}$ for a MNHA and $\mathbf{k}_{\mathrm{mode}}$ for a DNHA (compare with equations 2.5 and 2.6). We can describe this mathematically with an optical resonator, as in reference [15]. The model from this reference applies to a lossless system. In chapter 5 this model will be shortly presented. Next, we will extend it to include losses from the system. Figure 2 shows this model schematically. The model comes down to quantifying

the interference between the non-resonant (direct) channel and the resonant (indirect) one.

The problem of interference between a continuum of modes (direct process) and a single resonant mode (indirect process), has been solved for the first time by Fano, albeit in a completely different context [16]. The result is known as a Fano resonance: an asymmetric resonance, having a resonant frequency, ω_0, a lifetime, τ and an asymmetry q. Since at both types of arrays there is interference between a direct and an indirect contribution in the transmission, we expect the transmission spectra to consist of an overall background signal, modulated with spectrally well-determined, asymmetric Fano resonances that strongly depend on the angle of incidence (in equation 2.7 $\mathbf{k}_{//}$ is a function of angle of incidence).
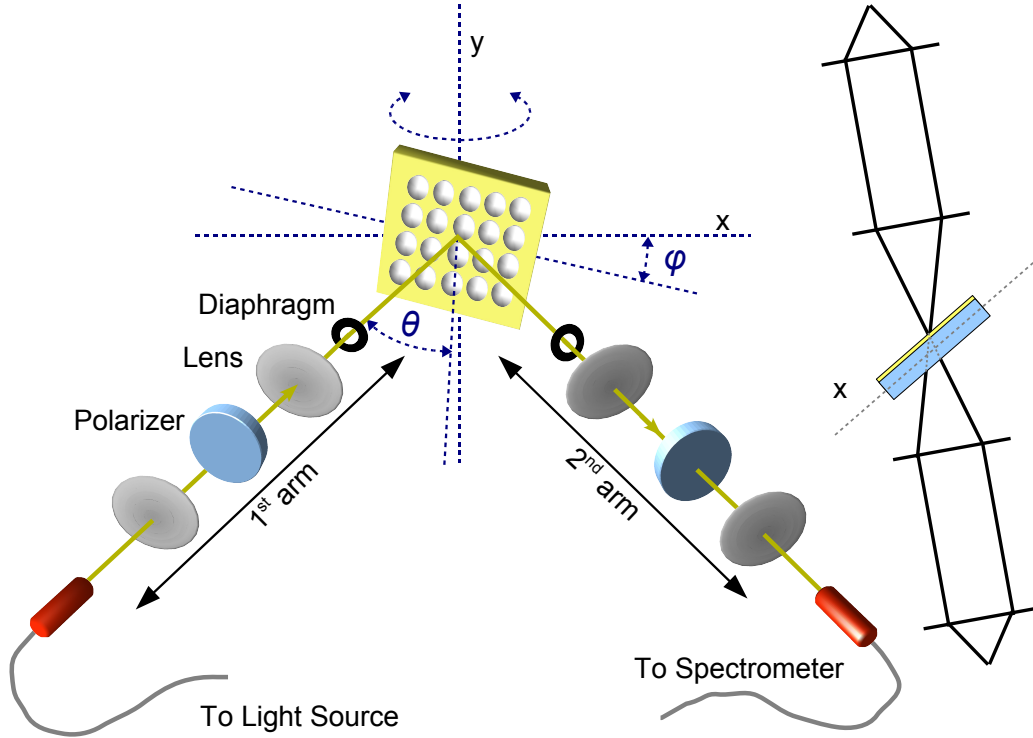
Figure 3: The setup shown schematically. The first arm allows us to focus white light under any linear polarization onto the sample. We are able to adjust the second arm in such a way, that we can measure both transmission and reflection spectra. θ corresponds to the angle of incidence, φ to the orientation of the sample. In the top right corner a top view of the setup in transmission mode is shown schematically.

3 Description of the Setup

To investigate the interaction between light and a nano-hole array we use a reflection-transmission setup, as shown in figure 3. We use a fiber-coupled tungsten lamp as a white light source. With a lens the light is focussed into a multimode fiber, unless otherwise specified the diameter of this fiber is $200\,\mu\mathrm{m}$. The light emitted at the end of the fiber is collimated by a lens with a focal distance of $50\,\mathrm{mm}$. The parallel beam of white light is polarized by a Glan-Thompson polarizing cube, with a spectral range of 300 to $2500\,\mathrm{nm}$. The angle of this polarizer can be adjusted to a precision better than $1°$. The beam is focussed onto the sample by a second lens with a focal distance of $75\,\mathrm{mm}$. The spot size on the sample has a diameter of $300\,\mu\mathrm{m}$ (a magnification of 1.5). After the lens a diaphragm allows us to adjust the numerical aperture (NA). The distance between the diaphragm and the sample is $60\,\mathrm{mm}$, and we can set the diameter of the diaphragm to less than $1\,\mathrm{mm}$, limiting the numerical aperture to less than 0.02, allowing us to treat the incident light as plane waves. The light path from the fiber until the diaphragm, we shall refer to as the first arm. We can set both the angle of incidence, θ,
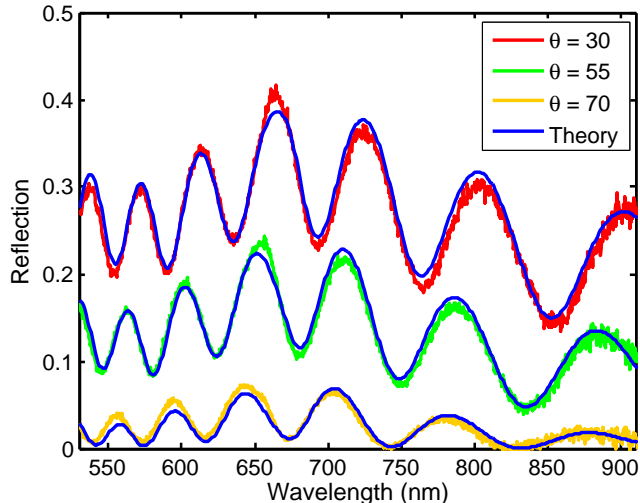
Figure 4: Reflection spectra of a multilayer sample with p-polarized light under various angles of incidence. The theoretical curves correspond very well to the measured ones, from which we may conclude that our setup is well aligned.

and the rotation angle of the sample, φ, with a precision of less than 1 degree.

We collect the reflected or transmitted light with a second arm, which is identical to the first arm. Depending on whether we want to measure reflection or transmission spectra, the angle of the second arm with respect to the first arm is 2θ and 180° respectively. The light at the end of the second arm is collected by a multimode fiber with a diameter of 400 µm. To analyze the visible part of the spectrum (530 till 910 nm), we use a fiber-coupled spectrometer with a CCD-array (Ocean Optics USB2000; resolution $\sim$ 1 nm). For the infrared part of the spectrum (910 till 1700 nm) we use a fiber-coupled spectrometer with a linear InGaAs array (Ocean Optics NIR-512; resolution $\sim$ 3 nm).

To calibrate the setup we measure reflection spectra of a known sample at several angles of incidence and compared them to calculated reflection spectra. The sample consists of three parallel layers: a 150 ± 10 nm thick $Ga_{0.35}Al_{0.65}As$ top layer, a 900 ± 20 nm thick AlAs layer, and a GaAs substrate. Theoretical reflection of this multilayer system as function of wavelength and angle of incidence were calculated [17], taking the dispersion of the materials into account [18]. Figure 4 shows both the measured and theoretical curves, showing very good agreement.

3.1 Samples

We investigate four different samples: a conventional gold nano-hole array (GNHA) [19], two GNHAs with a pillar placed in each hole, and a DNHA. The conventional GNHA is a 1×1 mm^2 perforated 200 nm thick gold film with square lattice symmetry. The diameter of the holes is 200 nm, the lattice constant 700 nm. The film is deposited on top of a glass substrate (Schott-BK7), with a refractive index of n $\approx$ 1.51 that is almost independent of wavelength for the range of wavelengths used in the experiment. Between the film and the substrate is a 2 nm thick Ti bonding layer. The sample is made with e-beam lithography. Further details of the production procedure of this sample can be found in reference [20].

We investigate two GNHAs with $\sim$ 650 nm long pillars sticking out of each hole. The
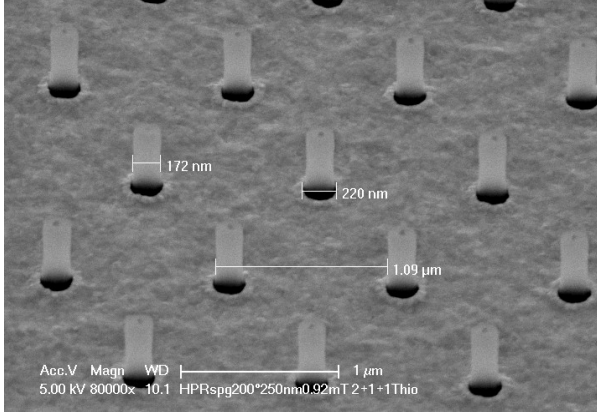
Figure 5: SEM image of the the gold nano-hole array with hexagonal symmetry. The holes and the pillars are 220 nm and 172 nm in diameter respectively. Each hole contains a 650 nm high glass pillar. The array has a lattice constant a = 1.09 µm.

samples are produced using an imprinting technique. The arrays are $0.5 \times 0.5\,\text{mm}^2$ perforated 200 nm thick films, deposited on an AF45 glass substrate, having an almost flat dispersion, n ≈ 1.52. Between the film and the substrate is a 100 nm thick layer of sol-gel glass with a refractive index of n ≈ 1.41. One of the arrays has square symmetry, the other one hexagonal symmetry. We will refer to them as 'Philips Square' and 'Philips Hexagonal', respectively. The array with square symmetry has a lattice constant of 760 ± 4 nm and a pillar thickness of 132 ± 5 nm. Figure 5 shows a SEM image of the GNHA with hexagonal symmetry. The lattice constant is 1090 ± 6 nm, the pillar thickness of 172 ± 5 nm and the hole diameter 220 nm. After optical studies of both the samples, the pillars are selectively removed using hydrofluoric acid. The sample then becomes a conventional GNHA. After optically investigating the samples without the pillars, a thin sol-gel glass layer is deposited on top of the array, with a refractive index, n ≈ 1.41. Further details of the production steps of these two samples can be found in reference [6], which is included in the appendix.

The DNHA is a $0.32 \times 0.32\,\text{mm}^2$ GaAs array with square lattice symmetry. The diameter of the holes is ∼ 200 nm, their depth $1.5 - 2$ µm. The lattice constant is 320 nm. Details of how this sample is produced can be found in reference [8].

4 Results and Analysis Gold Array

In this chapter results of optical transmission measurements on different types of GNHA's are presented. In the first three sections results obtained with the two Philips samples, as described in the previous section, are discussed. In section 4.1 measurements after removal of the glass pillars from these samples are analyzed. Without pillars the sample is in fact a conventional GNHA. The model from section 2.1 is applied. Next, in section 4.2, measurements on the same samples before removal of the pillars are presented and the effect of the pillars is studied. In section 4.3 results obtained with the SiO$_2$-coating on top of these Philips samples are presented. In the last section of this chapter measurements at the conventional GNHA, as described in the previous section, are investigated. The GNHA is immersed in liquids with different refractive indices.

4.1 Conventional GNHA

Figure 6(a) shows measured optical transmission spectra from an angle of incidence $\theta = 0°$ to $\theta = 15°$ with an interval of 1.5°. The used GNHA is 'Philips Square' as described in section 3.1, after removal of the pillars (note that then it is just a conventional GNHA). The incident light is p-polarized and the angle φ is set to 0°, see figure 3. The spectra show several peaks due to the coupling to SPPs. As expected, the peaks show a Fano shape due to the interference of the non-resonant direct, and mode-like indirect contribution in the transmission. This is in accordance with previous results [21].

As explained in section 2.1, two direct physical processes contribute to the optical transmission: transmission through the gold film and through the holes. The former can be calculated with equation 2.1. The thickness, d, of the GNHA is 200 nm (the thickness of all our used GNHA's is in fact 200 nm). According to reference [18], in the regime 200 nm $< \lambda < 1800$ nm the ratio $\kappa/\lambda > 3.5 \cdot 10^6$ m^{-1}. For these wavelengths the contribution in the transmission can now be calculated to be $T \leq 0.015\%$, which is negligible compared to the observed transmission. Therefore the contribution of this process can be neglected. The other direct process, the transmission through the holes, can be calculated with 2.2 and is plotted as function of wavelength in figure 7. If we compare this to figure 6, we see that the transmission is in the same order of magnitude.

Furthermore we can investigate the spectral positions of the resonances by applying the model from section 2.1. For this purpose it is convenient to plot the spectra from 6(a) in the form of a false color plot, as shown in panel (b). The color indicates the transmission as a function of wavelength and angle of incidence, high transmission is indicated with yellow, low transmission is indicated with black. To obtain a smoother plot we linearly interpolated the data five times between every 0.5 degree. The measured GNHA has a square lattice symmetry, so: $\mathbf{G} = k_a(N_1\hat{\mathbf{x}} + N_2\hat{\mathbf{y}})$. Here $k_a \equiv 2\pi/a \equiv \omega_a/c$, $\hat{\mathbf{x}}$ and $\hat{\mathbf{y}}$ are the reciprocal lattice vectors, and N_1 and N_2 are integer indices that count the number of oscillations per lattice period. The angular frequency of the incident light equals the angular frequency of the SPPs, $\omega_{\text{SPP}} = \omega$. We define our axes as shown in figure 3 and set $\varphi = 0°$. This allows us to rotate our sample around the $\hat{\mathbf{y}}$-direction, making $\mathbf{k}_{//} = |\mathbf{k_i}|\sin(\theta)\hat{\mathbf{x}}$, with $\mathbf{k_i}$ the wavevector of the incident light. If we substitute
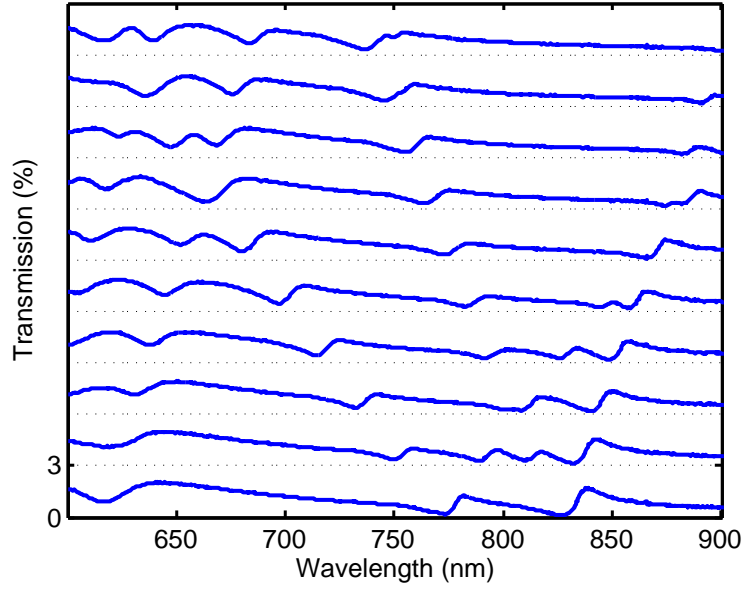
(a)
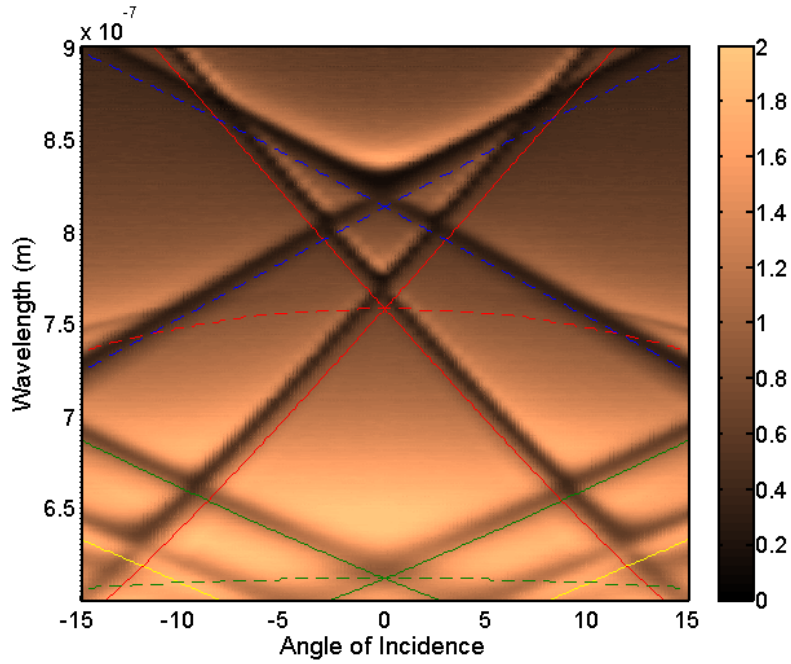
(b)

Figure 6: Panel (a) shows the transmission spectrum of a GNHA, under angles of incidence from 0° to 15°, with an interval of 1.5°. Panel (b) shows a plot of the wavelength against the angle of incidence, the color indicates the percentage reflected light. The curves show the theoretically expected resonant modes, calculated with equation 4.1; the blue dashed line corresponds to the (1,1)glass-mode, the red solid line to the (1,0)air-mode, the red dashed line to the (0,1)air-mode, the green solid line to the (2,0)glass-mode, the green dashed line to the (0,2)glass-mode and the solid yellow line to the (1,1)air-mode.

13
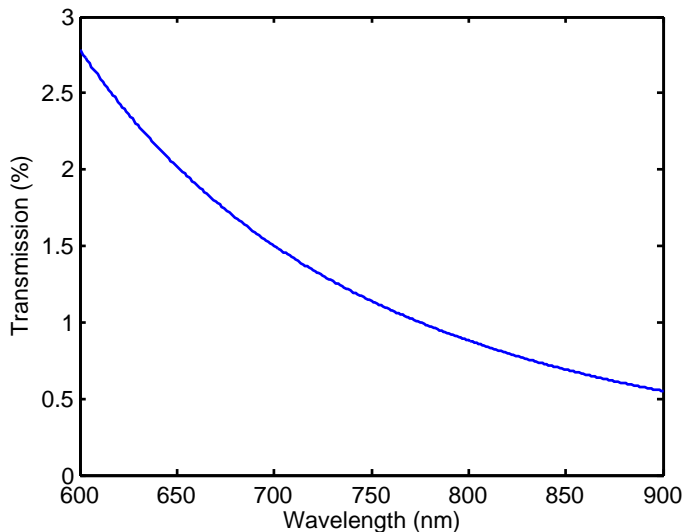
Figure 7: Theoretical transmission spectrum of a GNHA with a lattice constant, a, of $760\,\text{nm}$ and a hole diameter, d of $220\,\text{nm}$, as calculated with Bethe theory.

all this into equation 2.3, we obtain the following equation:

$$\left(\sin^2\theta - \text{n}_{\text{eff}}^2\right)\omega^2 + \left(2N_1\omega_a\sin\theta\right)\omega + \left(N_1^2 + N_2^2\right){\omega_a}^2 = 0. \tag{4.1}$$

This equation reveals how the quantization of the reciprocal lattice implies quantized resonances: each combination of N_1 and N_2 corresponds to a resonance. Also, every combination of N_1 and N_2 appears at both the gold-glass interface and the gold-air interface. Each solution corresponds to a mode, for instance: the $N_1 = 1, N_2 = 0$ solution at the glass interface we shall refer to as the (1,0) glass-mode. In principle we can solve this second order polynomial for the frequency exactly. However, the dielectric constant of gold depends rather strongly on the frequency. Taking this dispersion into account, this equation can be solved numerically, using exact data for the dielectric constant of gold [18] and approximating the effective refractive index of the substrate with a constant of 1.46. Recall that in fact the refractive index of the substrate is 1.52, and there is a $100\,\text{nm}$ sol-gel glass layer with a refractive index of 1.41 between this substrate and the gold film. Figure 6(b) shows the calculated spectral positions of the resonances as function of angle of incidence of the incident light. There is good agreement between the theoretically predicted curves and measured positions of the resonances. However, there is a slight systematic deviation; the measured resonances are shifted by $\sim 3\%$ towards the infrared compared to the model. This shift is observed in previous measurements [20] and by another group as well [22], although in our case the deviation is smaller because we take the dispersion of the refractive index of gold into account. The deviation may be due to several effects that are not taken into account in the model [20]. In the first place the SPP dispersion relation (equation 2.3) we used, is that of a closed, smooth gold-air interface, whereas in the GNHA the surface is perturbed with holes. In addition, the resonances are Fano shaped due to the interference of the resonant with the non-resonant channel. The actual positions of the peaks of the underlying resonances, which this model only considers, will therefore shift.

14
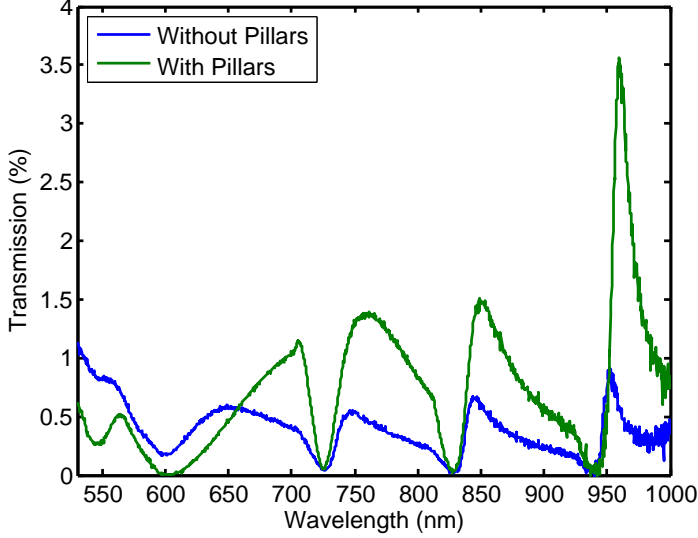
Figure 8: The green and the blue graph show the transmission spectra of a GNHA with pillars and after removal of the pillars, respectively.

4.2 Effect of Pillars

In this section it is investigated how the interaction between light and a GNHA changes when a pillar is placed in each hole of the array. To investigate the effect of the pillars, we measure the optical transmission through the GNHA's 'Philips Square' and 'Philips Hexagonal', before and after removal of the pillars, as described in section 3.1. It was found that the pillars increase the transmission by a factor of ~ 2 [6]. Also, the pillars increase the interaction between plasmon modes, resulting for normal incidence in an observed splitting $\Delta\omega/\omega \approx 6\%$ between the $(\pm 1, 0)$ air-mode for the array with pillars. For the array without pillars no splitting at all is observed for these modes [6]. In this section additional measurements on 'Philips Hexagonal' are discussed and compared to the results obtained with 'Philips Square'.

Figure 8 shows transmission spectra for normal incidence using p-polarized incident light, before and after removal of the pillars. The sample is oriented in such a way that the projection of the incident wavevector on the sample, $\mathbf{k}_{//}$, points in the same direction as one of the real lattice directions. We observe the same type of asymmetric Fano-shaped resonances as for the sample with square lattice symmetry. Again, the position of the resonances does not depend on the pillars. The transmission decreases significantly when the pillars are removed. This effect may partly be attributed to the fact that the pillars have a higher refractive index than air, reducing the wavelength and effectively making the holes larger. The observed change in peak transmission at $950\,\mathrm{nm}$ is a factor ~ 3.5.

The expected spectral location of the resonances as function of angle of incidence and wavelength of the incident light can again be calculated with equation 2.5. Now the measured GNHA has a hexagonal lattice symmetry, so: $\mathbf{G} = k_a[N_1\hat{\mathbf{x}} + \frac{1}{2}N_2(\sqrt{3}\hat{\mathbf{y}} + \hat{\mathbf{x}})]$. Following the same procedure as for the square array we find:

$$\left(\sin^2\theta - \mathrm{n}_{\mathrm{eff}}^2\right)\omega^2 + \left(\sqrt{3}N_1\omega_a\sin\theta\right)\omega + \left(N_1^2 + N_1 N_2 + N_2^2\right)\omega_a{}^2 = 0 \qquad (4.2)$$

15

Figure 9(a) and (b) show measured transmission spectra of the sample before and after removal of the pillars respectively, in the form of a false color plot, from an angle of incidence $-15°$ to $15°$ with an interval of $0.5°$. To obtain a smoother plot, we linearly interpolated 5 times between each measured angle. The curves are the theoretically predicted spectral positions of the resonances, obtained by numerically solving the above equation, again taking the dispersion of the refractive index of the gold into account [18]. As for the investigated samples with square lattice symmetry, there is good agreement between the model and the experiment. If we compare panels (a) and (b) the same effects as observed for the square lattice appear. For the sample without pillars, the $(0, \pm 1)$ air-modes are absent for small angles and the $(\pm 1, 0)$ air-modes are uncoupled. When a pillar is placed in each hole, the degenerate $(0, \pm 1)$ air-modes are apparent for small angles of incidence. The $(\pm 1, 0)$ air-modes now do show coupling at small angles of incidence. They split into two non-degenerate modes that show an avoided crossing. Contrary to the sample with the square symmetry, the glass mode does not obscure the avoided crossing. However, all the modes have shifted towards the infrared due to the larger lattice constant. This results in a very low transmission (recall that for the indirect process $T \sim 1/\lambda^4$, see equation 2.2). Figure 10 also shows the infrared part of the false color plot of figure 9(a). Because of the lower sensitivity of the IR-spectrometer, data with wavelengths larger than $1000\,\text{nm}$ suffer from a lot of noise. We attribute the observed discontinuity at this wavelength to the fact that transmission is lower than the sensitivity of the IR-spectrometer. This makes it hard to investigate the splitting of the $(1, 0)$ air- and $(-1, 0)$ air-mode, which is exactly around this point. The IR minimum of the resonance is estimated at $1005 \pm 10\,\text{nm}$, the visible minimum at $940 \pm 2\,\text{nm}$, corresponding to a splitting of $7.5 \pm 2\%$. The fill fraction of the sample is $(\pi d^2)/(2\sqrt{3}a^2) \cdot 100\% = 2.3\%$.

Although hard to observe, the $(0, \pm 2)$ glass-modes seem behave slightly different for a square array compared to a hexagonal one. This can be seen when we compare figure 6(b) to 9(a). Contrary to the square array the $(0, \pm 2)$ glass-modes now are apparent for very small angles, then disappear, to show up again at angles of $\sim \pm 10$ degrees. This is indicated with the white circles in figure 9(a). We do not know what causes this different behavior. However, when a pillar is placed in each hole, nothing changes for these glass modes, implying that it does not have anything to do with the antenna effect of the pillars. For comparison it would be convenient to see whether this effect is apparent at the air interface as well, however the $(0, \pm 2)$ air-modes are too far in the blue part of the spectrum to be observed.

4.3 Effect of Thin Glass Layer

In this section the effect of a thin glass layer on top of a GNHA is investigated. The sample we use is 'Philips Hexagonal', the same one as the one from the previous section. After the optical characterization of this sample with pillars, and after removal of the pillars, a thin glass layer is coated on top of the gold array. The sample now consists of a glass substrate with an optically thick gold film with perforated nano-holes in a regular pattern, and on top of this a $\sim 460\,\text{nm}$ thick layer of sol-gel glass. Figure 11(a)
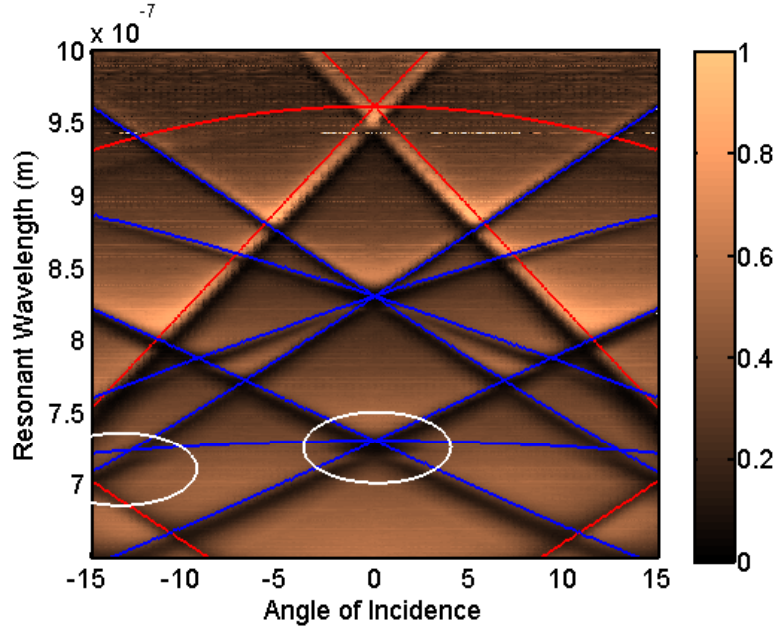
(a)
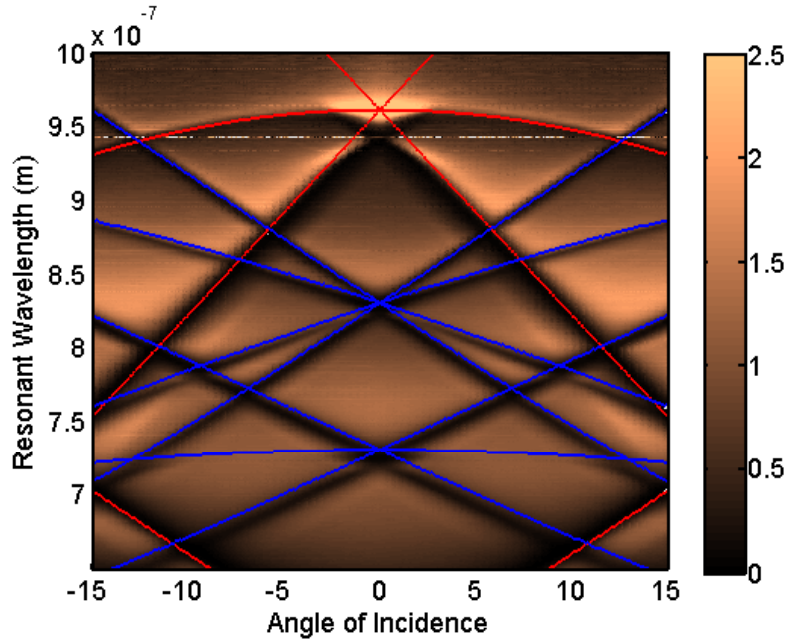
(b)

Figure 9: Both panels show a plot of the wavelength against the angle of incidence, the color indicates the percentage transmitted light. The curves show the theoretically expected resonant modes, calculated with equation 4.2. The blue lines correspond to glass-modes, the red lines to air-modes. The $(1,0)$ and $(-1,0)$ air-modes are indicated by the red graphs that go approximately linear with the angle of incidence and cross each other at normal incidence at a wavelength of $\sim 950\,\text{nm}$. The degenerate $(0,\pm 1)$ air-modes are indicated with the other red graph that crosses this point. The degenerate $(0,\pm 2)$ glass-modes are indicated with the blue graph that is $\sim 720\,\text{nm}$ at normal incidence and approximately constant at small angles.

17
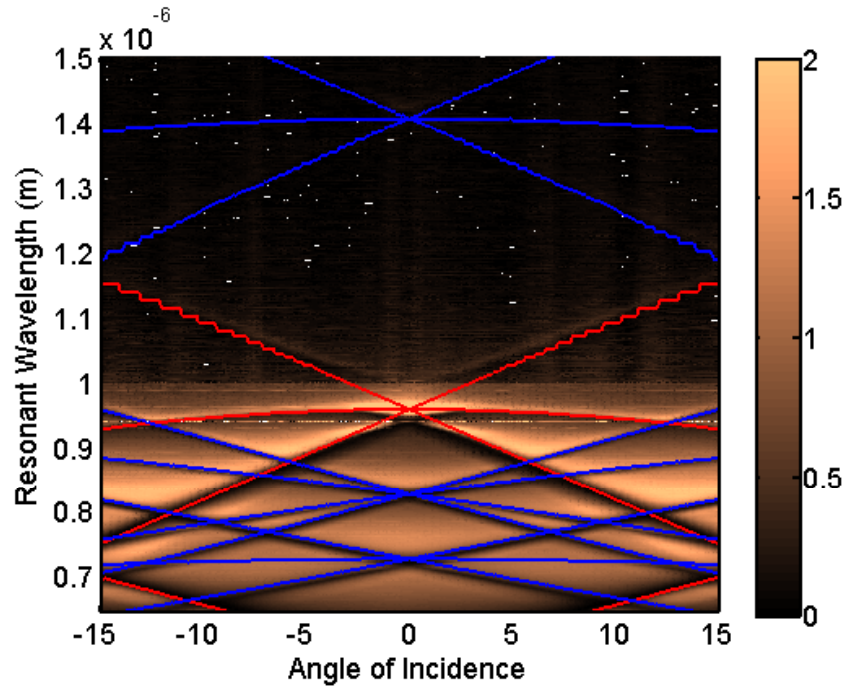
Figure 10: False color plot of the same data as the previous figure, but now the infrared part of the spectrum is shown as well. This infrared part is very noisy due to the low transmission and the relative low sensitivity of spectrometer. This makes it hard to accurately determine the spectral position of (the minimum of) the IR part of the resonance of the $(\pm 1, 0)$ air-modes. The general shape of the avoided crossing of these modes is clearly visible.
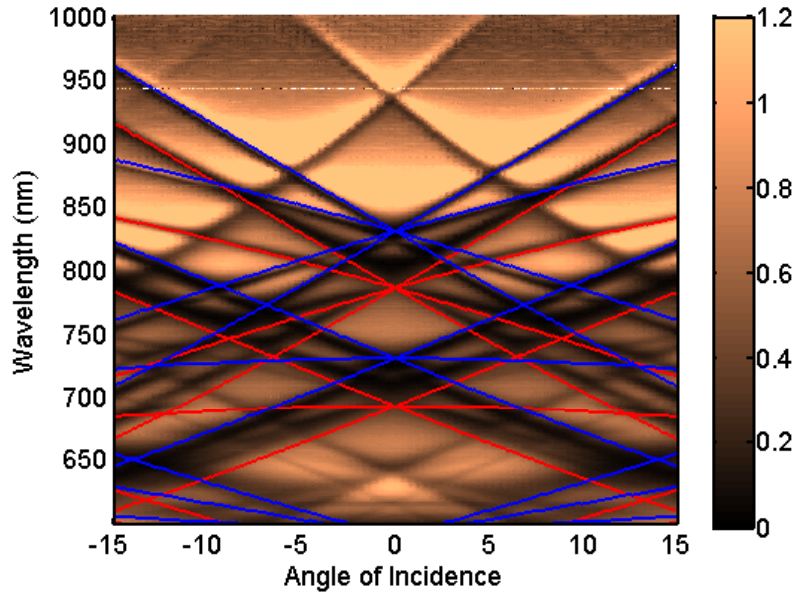
(a)
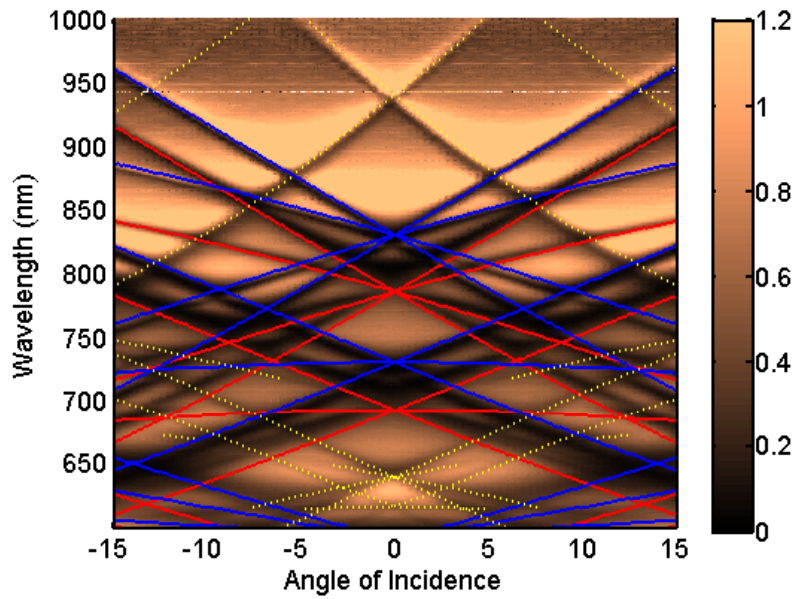
(b)

Figure 11: Panel (a) shows a false color plot of the same sample as the one from the previous graph, but with a thin layer of glass coated on top of the gold layer. The graphs are the modes calculated by solving equation 4.2 numerically. The blue ones correspond to SPP resonances at the substrate side and are in fact the exact same ones as the ones in figure 9. The red ones correspond to SPP resonances at the top side of the array and compared to the 'air' modes from before, they have shifted towards the glass-modes due to the higher refractive index of the coated glass compared to that of air. Also new modes occur, this is because the layer of coated glass supports waveguide modes. In panel (b) these observed resonances are indicated with (manually determined) yellow dotted lines.

19
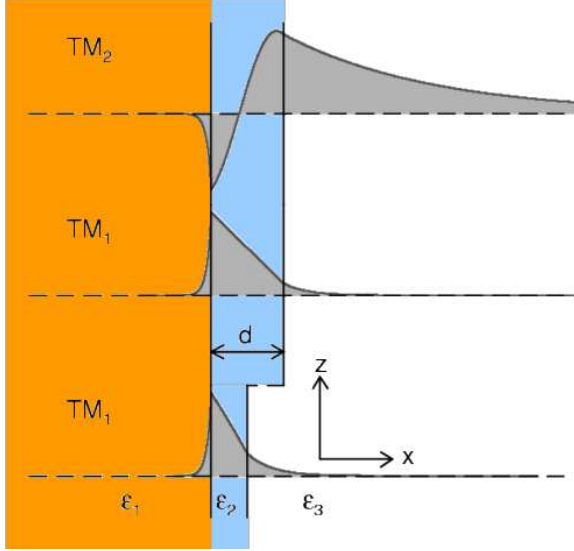
Figure 12: This figure shows a distribution of the electric field as a function of position. The lowest two graphs show surface plasmon modes that are bound to the interface. The top graph shows a waveguide mode, confined by internal reflection. The spectral position of each waveguide mode is quantified by the model presented in section 4.3.

shows transmission spectra, measured with p-polarized incident light at different angles of incidence in the form of a false color plot. The blue lines correspond to the plasmon modes at the glass side, and are in fact the exact same ones as the plasmon modes in figure 9. The plasmon modes that were initially on the air side have shifted towards the ones on the glass side because of the increased refractive index at this side of the sample. The blue curves are calculated with an effective refractive index of 1.41. Contrary to the previously presented measurements, not all the observed modes are due to SPPs. As can be observed from figure 11 new modes appear, as indicated with the yellow dotted lines in panel (b). The reason for the existence of these new modes lies in the fact that the coated layer of glass behaves as a waveguide. This behavior is shown schematically in figure 12. To quantify the spectral position of the modes as a function of angle of incidence, we apply the model presented in reference [23]. To find the k-vectors that are supported by the waveguide we numerically solve the following eigenvalue equations for s- and p-polarized modes respectively:

$$\tan(k_D d) = \frac{k_D(k_V + k_M)}{k_D^2 - k_V k_M}, \tag{4.3}$$

$$\tan(k_D d) = \frac{n_D^2 k_D(n_M^2 k_V + k_M)}{n_M^2 k_D^2 - n_D^4 k_V k_M}, \tag{4.4}$$

where d is the thickness of the sol-gel layer on top of the gold and n_D and n_M are the refractive indices of the dielectric and the metal respectively. Furthermore:

$$k_V = \sqrt{k_{\mathrm{EM}}^2 - (\omega/c)^2}, \tag{4.5}$$

$$k_D = \sqrt{(n_D \cdot \omega/c)^2 - k_{\mathrm{EM}}^2}, \tag{4.6}$$

$$k_M = \sqrt{k_{\mathrm{EM}}^2 - (n_M \cdot \omega/c)^2}, \tag{4.7}$$

with k_{EM} the parallel wavevector of the guided electro-magnetic mode. Equations 4.3 and 4.4 can be solved numerically. The number of solutions increases as the the sol-gel layer becomes thicker. Due to the lattice structure light can only couple to modes with certain $\mathbf{k}_{\text{EM}}$ vectors. For a hexagonal structure these modes are given by:

$$\text{Re}(\mathbf{k}_{\text{EM}}) = \omega/c\sin(\theta)\hat{\mathbf{x}} + \omega_a/c\left[N_1\hat{\mathbf{x}} + \frac{1}{2}N_2\left(\hat{\mathbf{x}} + \sqrt{3}\hat{\mathbf{y}}\right)\right], \tag{4.8}$$

where θ is the angle of incidence, $\omega_a = 2\pi/a$, with a the lattice constant, and N_1 and N_2 integers that count the number of oscillations per lattice period. The length of the real part can now be calculated to be:

$$\text{Re}(k_{\text{EM}}) = \frac{1}{c}\sqrt{\left[\omega\sin(\theta) + \omega_a(N_1 + N_2/2)\right]^2 + 3/4\left[\omega_a N_2\right]^2}. \tag{4.9}$$

The spectral positions of the resonances as function of angle of incidence are given by the intersections between the plane spanned by this equation and the plane(s) spanned by the the real part(s) of k_{EM} as from equations 4.3 and 4.4 for s- and p-polarized modes respectively. Figure 13 shows the results of solving this system of equations, using the above mentioned values for n_D, d and a, and again taking the dispersion of the gold, $n_M(\lambda)$ into account. The red lines correspond to the manually determined observed position of the resonances, they are the same as the yellow dotted lines in figure 11. The figure shows good agreement between the measured and the predicted spectral positions of the resonances, for both s- and p-polarized incident light. Some theoretically predicted modes are not observed in the measurements. This is partly due to the fact that some of the modes are obscured by the much stronger surface plasmon modes. Another reason is the polarization of the incident light. The measurement is performed with p-polarized incident light, making the excitation of the $(0, \pm N)$ TM-waveguide modes, with N and integer, very inefficient for small angles of incidence. In figure 13 these modes correspond to the black markers with limited dispersion, crossing normal incidence at ~ 700 and $\sim 945\,\text{nm}$.

The same measurements and analysis are also performed on the sample 'Philips Square'. Using the same values for n_D and d, good agreement between theory and experiment was found again [24].

4.4 Index Tuning

To investigate the effect of tuning the refractive index at the top-side of the sample we put a GNHA in several liquids with different refractive indices. For this experiment we use the conventional GNHA, as described in section 3.1. We use the following liquids: water, dimethyl sulfoxide (DMSO) and methoxybenzene (Anisole) with an index of refraction, n_D, of 1.33, 1.48 and 1.52, respectively [25]. Transmission measurements at normal incidence are shown in figure 14. As is accurately predicted by equation 4.2 the resonances at the liquid side of the GNHA shift towards the infrared part of the spectrum. For the index-matched case the index of refraction of the used liquid is the same as the index of refraction of the substrate. This is the case for Anisole: at both
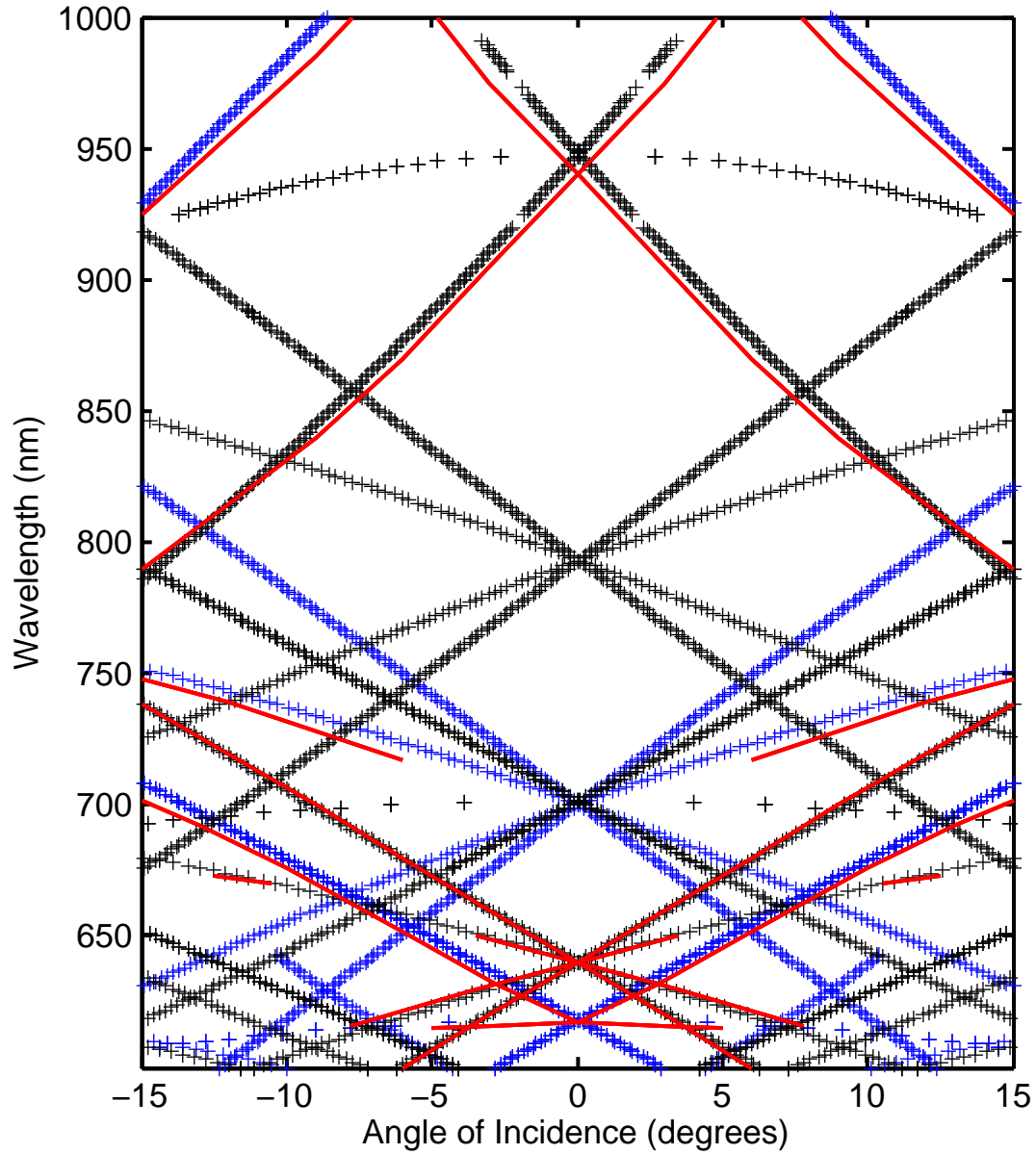
Figure 13: The observed waveguide-modes in panel (b) from the figure 11 are compared with the model presented in section 4.3. The red curves correspond to the observed resonances, indicated with the yellow dotted lines in panel (b) from the previous figure. The markers correspond to calculated modes: the blue ones, corresponding to *s*-polarized modes, describe the intersection between the planes spanned by equations 4.3 and 4.9, the black ones, corresponding to *p*-polarized modes, between the planes spanned by equations 4.4 and 4.9.
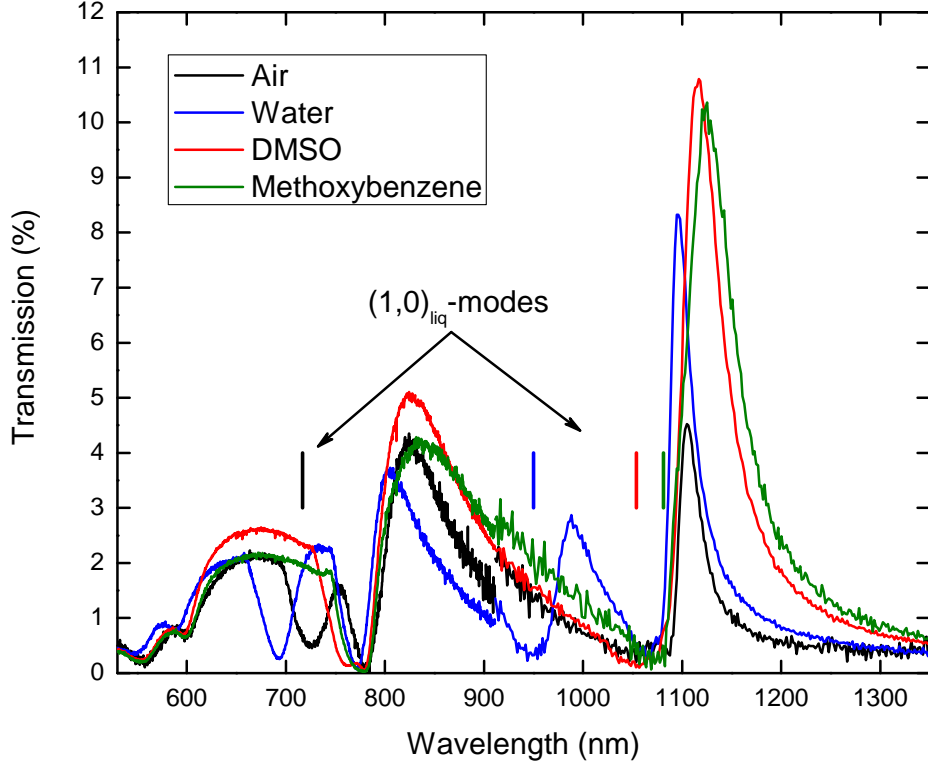
Figure 14: Transmission measurements at normal incidence. The discontinuity at 910 nm is due to the use of two spectrometers. The index of refraction at the gold side of the GNHA is tuned by using different liquids. As a result the modes that are apparent at this side of the sample shift towards the infrared part of the spectrum. The vertical stripes indicate the spectral positions of the $(\pm 1, 0)$- and $(0, \pm 1)-$modes at this side, as predicted with equation 4.1. Note that these modes are degenerate at normal incidence. In the index-matched situation the refractive index of the liquid is equal to that of the glass. The modes on both sides are indistinguishable and lie on top of each other.
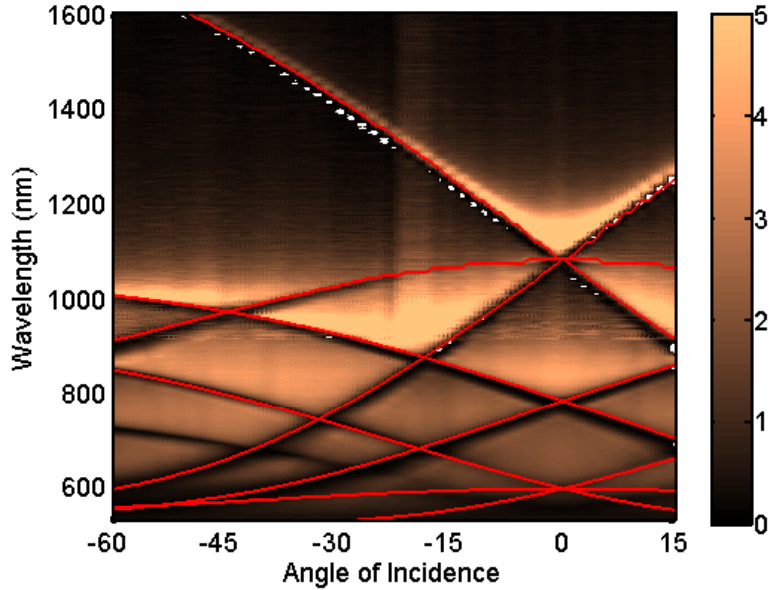
Figure 15: A false color plot of a conventional GNHA immersed in an index-matching liquid, measured with *p*-polarized incident light. The color indicates the percentage of the transmitted light. The modes at both sides of the array have shifted exactly on top of each other. The red lines indicate the $(-2, -2)$- to the $(2, 2)$-modes, calculated with equation 4.1.

sides $n_D = 1.52$. Figure 15 shows spectra measured under angles of incidence from $-60°$ to $15°$ as a false color plot. It shows that the modes propagating at both sides of the array have shifted exactly on top of each other.

The resonance is still accurately described by a Fano resonance, as one would expect because of the interference between the direct and the indirect contribution in transmission [21]. This is confirmed by figure 16, where one of the resonances is fitted with a function that describes a Fano shape [16]:

$$T = \frac{(\omega - \omega_{\mathrm{res}} + q)^2}{(\omega - \omega_{\mathrm{res}})^2 + C}, \tag{4.10}$$

with ω_{res}, q and C free fitting parameters. Note that it is hard to isolate a single resonance, because of the length of the tail of each resonance and the fact that there are a lot of resonances apparent. In this case, below 1050 nm another mode starts to contribute to the signal obscuring this resonance, as can be observed from figure 14. In principle we could fit with the sum of multiple independent Fano resonances, resulting in a more accurate fit. However, the amount of fit parameters also increases drastically.
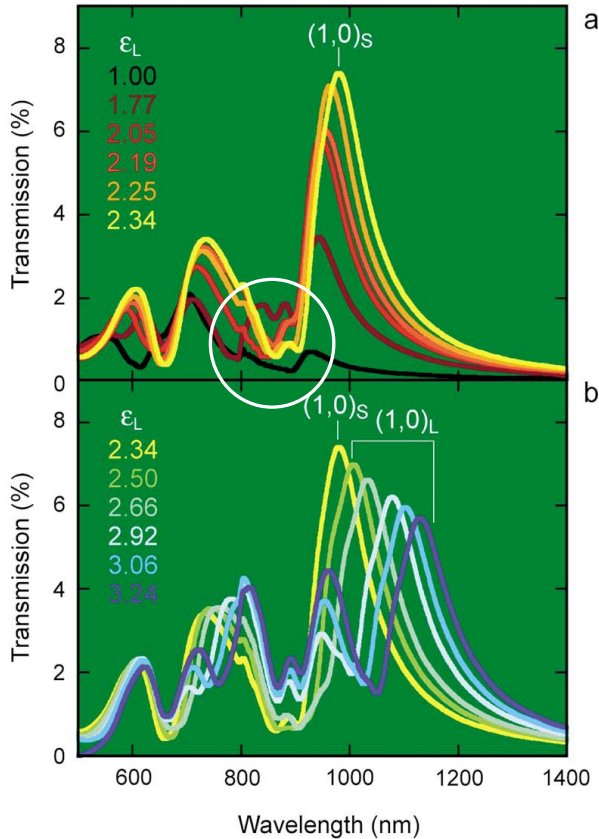
Figure 17 shows the enhancement in transmission of both the maximum of the $(\pm 1, 0)$ liquid- and $(0, \pm 1)$ liquid-modes and the average transmission between 530 and 1350 nm. The enhancement in the peak transmission is ~ 2.5 for the index-matched situation, being significantly more than a factor of 2, the amount one could expect if the modes
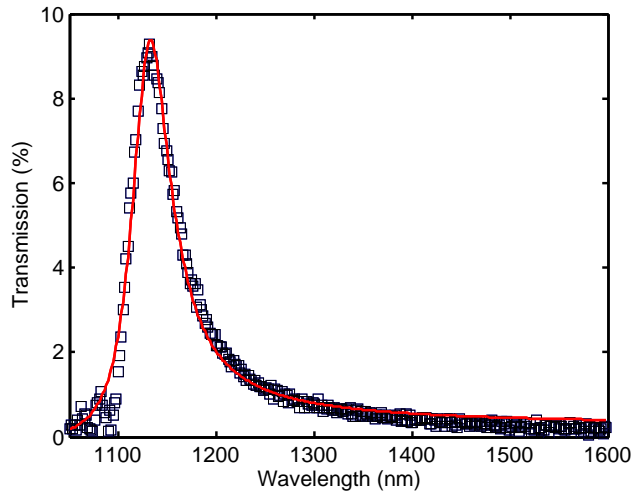
Figure 16: The data are the same as the data of the green graph in figure 14. As the fit shows, the shape of the data can be accurately described by a Fano resonance. This effect occurs due to the interference between the contribution of the direct and the indirect channel.
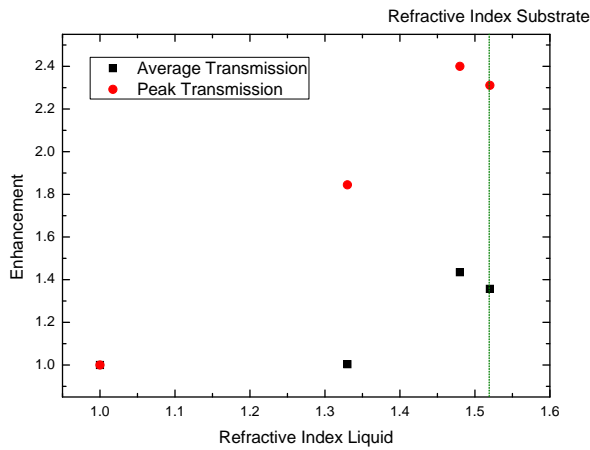
Figure 17: The red graph corresponds to the enhancement in the maximum transmission of the peak corresponding to the $(\pm 1, 0)$- and $(0, \pm 1)$ liquid modes. The black graph shows the enhancement in the average transmission between 530 and 1350 nm. The green dotted line corresponds to the refractive index of the substrate.

25

Figure 18: Measured data from reference [26]. They claim to observe a factor ~ 10 enhancement in the transmission through a GNHA, whereas we observe a factor ~ 2.5 enhancement. Reasons for this discrepancy are explained in the text.

at both sides of the array were completely uncoupled. However, contrary to claims from reference [26], it is far from the their claimed observed factor of 10. Figure 18 shows their measured data. We attribute this discrepancy to two reasons. In the first place they performed their measurements with a much too large numerical aperture. This can immediately be observed from figure 18 with the experimental data. A little 'bump' occurs at $\sim 900\,\mathrm{nm}$ instead of the 'hard zero' that should occur due to destructive interference between the direct and the indirect contribution, as is for example confirmed by figure 8. This bump is in fact the $(\pm 1, 0)$-glass mode integrated over a small, but significant range of angles. In the second place they are not justified to treat their nano-hole arrays as an infinitely large array. The fact that the arrays they use are so small (only 17×17 holes) results in diffraction effects, probably obscuring the effects they claim to investigate.

The enhancement in the average transmission also seems to confirm that there is some form of coupling between the modes propagating at the two sides of the array. However, at the same time more modes at the liquid side have shifted towards the IR part of the spectrum. This also contributes to a higher average transmission. For a more detailed investigation of the coupling between the two sides of the GNHA, further research with more liquids with different indices has been performed. Results of this analysis are published in a paper [7] that is attached in the appendix.

In the next chapter the model from reference [15] will be extended. This model is based

26

on the idea that the interaction of light with a nano-hole array that is symmetric in the plane parallel to the lattice, can be described with an optical resonator. It assumes that there is a direct, non-resonant contribution in the transmission and an indirect, resonant one. By introducing a third channel, leaks from the system can be taken into account. This model in principle also applies to the index-matched case of a GNHA. Here, the transmission through the direct channel corresponds to the transmission directly through the holes. The transmission through the resonant, indirect channel corresponds to light that is diffracted by the lattice and excites SPPs. The SPPs can couple to the other side of the array and can be emitted as photons again. The loss channel takes the evanescent character of the SPPs and the absorption of light into account. The fact that the refractive indices at both sides of the array is the same guarantees the symmetry of the system on which the model from reference [15] is based. In principle we can calculate the reflection (the transmission can be calculated in a similar way) with equation 5.12, if we would have accurate values for r and t, the reflection and transmission coefficients of a single interface respectively. Here the first problem occurs, namely that the phase of these coefficients depends on the complex part of the refractive index of gold, which is a rather wild function at the wavelengths that we want to investigate. A second problem arises due to the fact that the leak is in this case related to the absorption of light by the gold. This also depends on the complex part of the refractive index of gold. Therefore this is strongly varying as a function of the wavelength of the incident light. The model explicitly assumes that the loss channel is independent of the wavelength (Λ is a wavelength independent fitting parameter).

5 Results and Analysis Dielectric Array

In this chapter results of different types of reflection measurements on a DNHA are presented and analyzed. Technical details of this sample can be found in section 3.1. In order to explain some of the observed phenomena, we extended the Fano model presented in reference by including absorption and scattering losses [15]. In this chapter, first the reflection measurements are described qualitatively, after which the Fano model is described and extended in order to analyze the measurements quantitatively. Finally, additional measurements are presented in which the sample is rotated around its axis, while keeping the angle of incidence constant.

5.1 Flipping Resonances

Figure 19 shows reflection spectra for different angles of incidence from 20° to 70°, with steps of 10°. The spectra are offset vertically for clarity. In these measurements the rotational angle ϕ is set to zero degrees, so that the polarization always points in the same direction as one of the lattice vectors. In panel (a) both the polarizer and the analyzer are set to s-polarization, in panel (b) to p-polarization. For both polarizations we observe a single peak at a wavelength of $\sim 950\,\mathrm{nm}$ on top of an oscillating background. The resonance varies with the angle of incidence, as does its shape. For s-polarized light (figure 19(a)) the resonance is observed to be asymmetric with a tail pointing towards the blue for every angle of incidence. For p-polarized light (figure 19(b)) the resonance behaves differently, the asymmetry flips. For angles of incidence below $\sim 70°$ the resonance is asymmetric with a tail pointing towards the red, at an angle of incidence of $\sim 70°$ it is symmetric, and for angles of incidence larger than $\sim 70°$ the tail points towards the blue.

5.2 Reflection and Transmission Coefficients

To calculate reflection and transmission coefficients that describe the direct process we approximate the DNHA with a homogeneous dielectric film. In terms of the angle of incidence of the incident light, θ, the known refractive index of the Gallium Arsenide DNHA, n_{GaAs} [18], and the thickness of the perforated layer ,d, the reflection and transmission coefficients of the film are respectively given by [27, 28]:
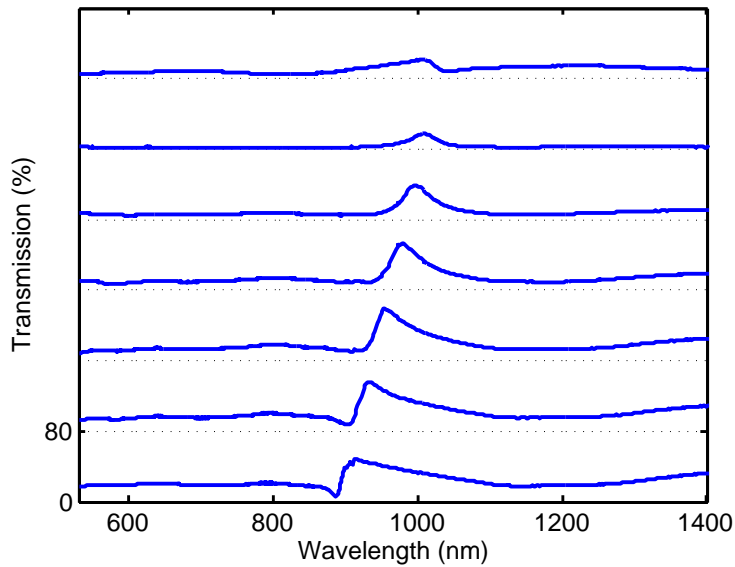
$$r = \frac{\Upsilon_0 m_{11} + \Upsilon_0 \Upsilon_{\mathrm{s}} m_{12} - m_{21} - \Upsilon_{\mathrm{s}} m_{22}}{\Upsilon_0 m_{11} + \Upsilon_0 \Upsilon_{\mathrm{s}} m_{12} + m_{21} + \Upsilon_{\mathrm{s}} m_{22}}, \tag{5.1}$$

$$t = \frac{2\Upsilon_0}{\Upsilon_0 m_{11} + \Upsilon_0 \Upsilon_{\mathrm{s}} m_{12} + m_{21} + \Upsilon_{\mathrm{s}} m_{22}}, \tag{5.2}$$

where $\Upsilon_0 = \cos(\theta)$, and $\Upsilon_{\mathrm{s}} = n_{\mathrm{GaAs}} \cos(\theta_{\mathrm{GaAs}})$ for s-polarized incident light and $\Upsilon_{\mathrm{s}} = \cos(\theta_{\mathrm{GaAs}})/n_{\mathrm{GaAs}}$ for p-polarized incident light, with $\theta_{\mathrm{GaAs}} = \arcsin(\sin(\theta)/n_{\mathrm{GaAs}})$. The coefficients m_{ij} are the elements of the transfermatrix of a homogeneous dielectric film [27]:
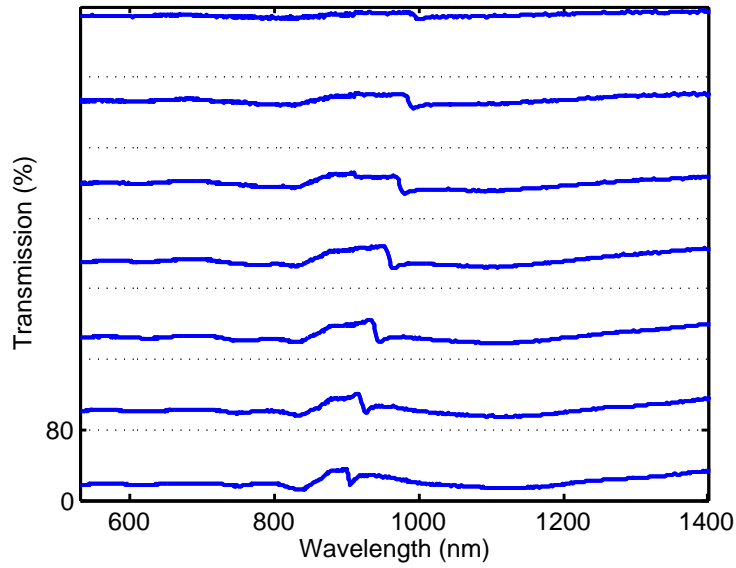
(a)

(b)

Figure 19: Both panels show reflection spectra under angles of incidence from 20° (bottom graph) to 80°, every 10°. Panel (a) shows data measured with *s*-polarized incident light, panel (b) with *p*-polarized incident light. In both cases the analyzer is set parallel to the polarizer. Both spectra show an angle dependent asymmetric resonance on top of an oscillating background. For the resonance measured with *s*-polarized light, the tail points towards the blue for all angles of incidence, for the one with *p*-polarized light the tail points towards the red for angles of incidence smaller than $\sim 70°$, becomes symmetric at $\sim 70°$ and points towards the blue for angles larger than $\sim 70°$.

29

$m_{11} = m_{22} = \cos(h)/\lambda$, with $h = 2\pi \text{n}_{\text{DNHA}} d \cos(\theta_{\text{DNHA}})$, where n_{DNHA} the effective refractive index of the perforated GaAs layer and $\theta_{\text{DNHA}} = \arcsin(\sin(\theta)/\text{n}_{\text{DNHA}})$. Furthermore, $m_{21} = -i\sin(h/\lambda) \cdot \Upsilon_{\text{DNHA}}$ and $m_{12} = -i\sin(h/\lambda)/\Upsilon_{\text{DNHA}}$, where for s-polarized incident light $\Upsilon_{\text{DNHA}} = \text{n}_{\text{DNHA}} \cos(\theta_{\text{DNHA}})$ and for p-polarized incident light $\Upsilon_{\text{DNHA}} = \cos(\theta_{\text{DNHA}})/\text{n}_{\text{DNHA}}$.

To get an estimate of the effective refractive index of the perforated GaAs layer, we use Maxwell-Garnett theory [29, 30]. In this theory the perforated layer is treated as a layer of lossless cylinders of subwavelength diameter, in a uniform, lossless medium. The effective refractive index can be calculated as a function of the polarization of the incident light. The advantage of this model is that it uses only the fill fraction of the cylinders (so the volume fraction of air and GaAs) as an adjustable parameter. For transverse electric (TE-) polarized light, the **E**-vector is perpendicular to the cylinders and for transverse magnetic (TM-) polarized light it points in the direction of the cylinders. The effective refractive indices of TE- and TM-polarized light are then given by:

$$
\begin{aligned}
\text{n}_{\text{eff}}^{TE} &= \text{n}_{\text{GaAs}}\sqrt{\frac{1+2\cdot f\cdot\alpha}{1-f\cdot\alpha}} \\
\text{n}_{\text{eff}}^{TM} &= \sqrt{f \cdot \text{n}_{\text{Air}}^2 + (1-f) \cdot \text{n}_{\text{GaAs}}^2}
\end{aligned}
\tag{5.3}
$$

with $f = 0.31$, the fill fraction and $\alpha \equiv (\text{n}_{\text{Air}}^2 - \text{n}_{\text{GaAs}}^2)/(\text{n}_{\text{Air}}^2 + \text{n}_{\text{GaAs}}^2)$, the polarizability. The refractive indices for both TE- and TM-polarized waves as a function of wavelength are plotted in figure 20. For s- and p-polarized incident light the effective refractive index of the perforated layer becomes respectively:

$$
\begin{aligned}
\text{n}_{\text{DNHA}}^s &= \text{n}_{\text{eff}}^{TE} \\
\text{n}_{\text{DNHA}}^p &= \text{n}_{\text{eff}}^{TE}\sqrt{1 + \sin(\theta)^2\left(\frac{1}{(\text{n}_{\text{eff}}^{TE})^2} - \frac{1}{(\text{n}_{\text{eff}}^{TM})^2}\right)}
\end{aligned}
\tag{5.4}
$$

The reflection and transmission coefficients can now be calculated with equations 5.1 and 5.2, as function of wavelength, angle of incidence and polarization.

5.3 Optical Resonator Model for a DNHA

In this section the most essential principles of the model from reference [15] are highlighted and applied to our measurements. In the next section this model will be extended for a more accurate description. The model treats the DNHA as a single-mode optical resonator with m ports, mathematically the same as a driven harmonic oscillator [11]. For this system the dynamic equations can be written as:

$$
\frac{da}{dt} = \left(i\omega_0 - \frac{1}{\tau}\right)a + (\langle\kappa|^*)\,|s_+\rangle, \tag{5.5}
$$

$$
|s_-\rangle = C|s_+\rangle + a|d\rangle, \tag{5.6}
$$

where a, ω_0 and τ are the amplitude, the angular frequency and the lifetime of the resonant mode respectively. The incoming waves and the coupling to the resonator are
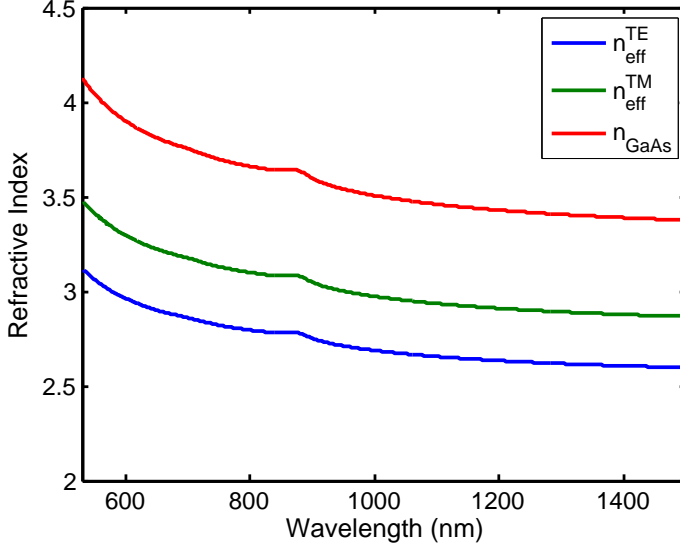
Figure 20: Real part of the effective refractive indices as a function of wavelength, calculated with equation 2.4, for a fill fraction $f = 0.31$. The complex part is zero for wavelengths larger than 900 nm. Note the birefringent character of the system.

described by the $m \times 1$ vectors $|s_+\rangle$ and $|\kappa\rangle$ respectively. The coupling to the outgoing field and the outgoing field itself are described by the $m \times 1$ vectors $|d\rangle$ and $|s_-\rangle$. C is the scattering matrix that describes the direct contribution. For a system with no inherent losses energy conservation and time reversibility impose several conditions:

- $\langle d|d \rangle = 2/\tau$;

- $|\kappa\rangle = |d\rangle$;

- $C|d\rangle^* = -|d\rangle$.

This allows us to write the scattering matrix of the total system, S, and the conditions it has to meet, in the following general form:

$$S = C + \frac{|d\rangle\langle d|^*}{i(\omega - \omega_0) + 1/\tau}, \quad \text{with furthermore} \quad \begin{cases} C|d\rangle^* = -|d\rangle \\ \langle d|d\rangle = 2/\tau \end{cases} \qquad (5.7)$$

For an exact mathematical description of this optical oscillator we need to solve this system of equations. However, for the general case this is unsolvable since we have $m+1$ equations and m complex unknown parameters.

A system that can be solved exactly is the symmetric two-port DNHA slab. In the first place we consider only two ports, so $|d\rangle = (d_1, d_2)^{\mathrm{T}}$. This simplification of the system allows us to rewrite C as follows:

$$C = e^{i\phi} \begin{pmatrix} r & it \\ it & r \end{pmatrix}, \qquad (5.8)$$

where r, the reflection coefficient, t, the transmission coefficient are real functions of the wavelength and can be calculated as in the previous section. The phase ϕ is a real number. Secondly, the material on both sides of the perforated layer is (optically) the same. This makes our system symmetric in the plane of the DNHA slab, demanding

31

that the diagonal elements of S are equal, so $d_1^2 = d_2^2$. These two extra relations allow us to write equation 5.7 as:

$$S = e^{i\phi} \left\{ \begin{pmatrix} r & it \\ it & r \end{pmatrix} + \frac{1/\tau}{i(\omega - \omega_0) + 1/\tau} \begin{pmatrix} -(r \pm it) & \mp(r \pm it) \\ \mp(r \pm it) & -(r \pm it) \end{pmatrix} \right\},$$ (5.9)

where the $\pm$ signs depend on whether we are considering an even or an odd mode with respect to the plane of the slab. From this the reflection, $R = |S_{11}|^2$, can be calculated to be:

$$R = \frac{r^2(\omega - \omega_0)^2 + t^2/\tau^2 \mp 2rt(\omega - \omega_0)/\tau}{(\omega - \omega_0)^2 + 1/\tau^2}.$$ (5.10)

This equation reveals some interesting properties of a reflection spectrum of a symmetric DNHA slab. It predicts a resonance on top of an oscillating background. Typically the resonance takes a Fano shape [16], due to the interference between both channels. Only in the case that either r or t is zero a Lorentzian shape is reproduced. In other words, when either one of the direct contributions is turned off, the interference disappears and therefore Fano shape vanishes. Furthermore the $\mp$ sign and the sign of the product of r and t, determine the orientation of the asymmetry of the Fano, so whether the tail points towards the blue or the red part of the spectrum. We can apply this model qualitatively to the modes in figure 19. For s-polarized incident light r has the same sign for all angles of incidence. Therefore the sign of the product of r and t is the same and the tail of the resonance points in the same direction, the blue, for all angles of incidence. For p-polarized incident light on the other hand, it is shown that at Brewster's angle, θ_B, the reflection coefficient r flips, from positive to negative. This explains why the asymmetry of the resonance flips at Brewster's angle: it has a tail towards the red for $\theta < \theta_B$, it is symmetric for $\theta = \theta_B$ and it has a tail pointing towards the blue for $\theta > \theta_B$.

To conclude, most of the observed phenomena, like the oscillating background and the flipping of the Fano at Brewster's angle, are predicted by this equation. However, there are also some discrepancies, for instance the fact that the minimum and the maximum of the resonance are always at 0% and 100%. In the next section we extend the model by introducing a loss channel to take this effect into account.

5.4 Loss Channel and Data

In order to get better agreement between the model and our experiment, we introduce a loss channel. This channel takes both scattering in the waveguide and diffraction that occurs due to the higher diffractive index of the substrate into account. The optical resonator is shown schematically in figure 2. We have to solve for the system of equations 5.7. If we assume no coupling occurs between the incident light and the loss channel, neglecting scattering from the incident light, we can rewrite the scattering matrix of the direct contribution as follows:

$$C = e^{i\phi} \begin{pmatrix} r_1 & t & 0 \\ t & r_2 & 0 \\ 0 & 0 & 1 \end{pmatrix},$$ (5.11)
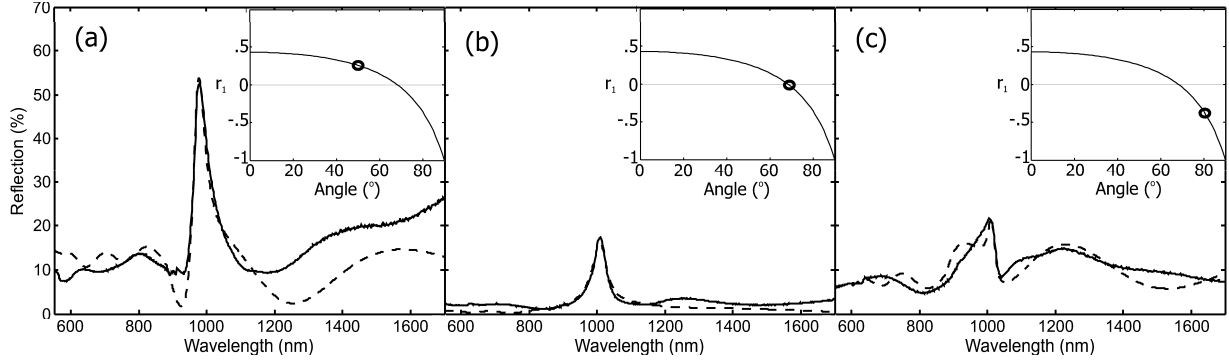
Figure 21: The solid lines indicate reflection spectra under angles of incidence of 50° (a), 70° (b) and 80° (c). The dashed lines are fits obtained with equation 5.12. The insets show the Fresnel reflection coefficient, r_1, for an interface between air and $n_{\text{eff}} = 2.5$ as function of angle of incidence. The circles indicate the value corresponding the measurement.

where the Fresnel coefficients, r_1, r_2 and t are now complex. In order to incorporate the losses in our model, we assumed that a factor Λ of the light entering the resonator leaks into the third, loss channel, or $|d_3|^2 = \Lambda \cdot 2/\tau$. Assuming the coupling from the resonator to the outgoing field to be the same at both sides of the perforated layer, again imposes the condition $d_1^2 = d_2^2$. Now the system of equations can be solved again and we can calculate the intensity reflection coefficient to be:

$$R = \left| \frac{i(\omega - \omega_0)r_1 \pm 1/\tau[\Lambda r_1 + (1 - \Lambda)t]}{i(\omega - \omega_0) + 1/\tau} \right|^2. \tag{5.12}$$

After setting the thickness and the fill fraction of the perforated layer, the Fresnel coefficients are fixed. There are three fit parameters left: the resonance angular frequency ω_0, the lifetime τ and the leakage to the third channel Λ. Figure 21 shows measured reflection spectra under three different angles of incidence, and fits with equation 5.12. The fill fraction was set once and Λ, τ and ω_0 were the only three free fitting parameters. Despite small quantitative deviations, qualitatively all phenomena are explained by the model. We attribute most deviations to the simplifications we made in the model. Maxwell-Garnett effective medium theory is only valid if the cylinders are much smaller than the wavelength of light. Also, the holes are not exactly cylindrical, as is clearly illustrated in figure 1(b) of reference [8]. Furthermore we assumed the coupling to both sides of the resonator to be equal, which is most probably not the case, as the coupling between the waveguide and the air side and the waveguide and the GaAs side is likely to be different.

5.5 Rotation with Crossed Polarizers

In this section we discuss the rotational dependency of the reflection. We measured reflection spectra at a fixed angle of incidence of 60°, while rotating the sample over 405°, with an interval of 3°. $\varphi = 0°$ corresponds to the (1,0)-direction, as shown in figure 3. The polarizer is set to p-polarization, the analyzer to s-polarization. A false

color plot of this measurement is shown in figure 22(a). The sample and the polarization of the incident light are mirror symmetric every 45 degrees in the plane being spanned by $\mathbf{k}$ and $\mathbf{k}_{//}$. This symmetry must be conserved in the reflected light, implying for figure 22 that the 'slices' $[-45°, 0°]$, $[45°, 0°]$, $[45°, 90°]$, $[135°, 90°]$ etc. should all be the exact same. Figure 22(b) shows measured reflection spectra from $\varphi = -315°$ to $\varphi = 90°$ with an interval of $45°$. Clear quantitative differences show up. In fact, for these angles, $0° \pm n \cdot 45°$ with n an integer, the symmetry of the system forbids any changes in polarization. Because the polarizers are crossed with respect to each other, the reflection should drop to zero. This is not the case, as shows up most strikingly for an angle of $-180°$. These observations seem to imply that we suffer from an asymmetry in our sample due to imperfections in the fabrication process.

(a)

(b)
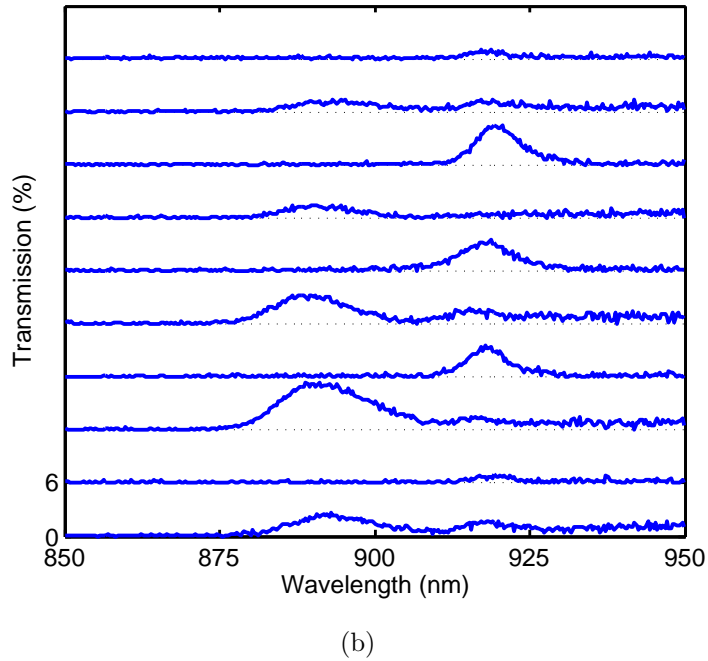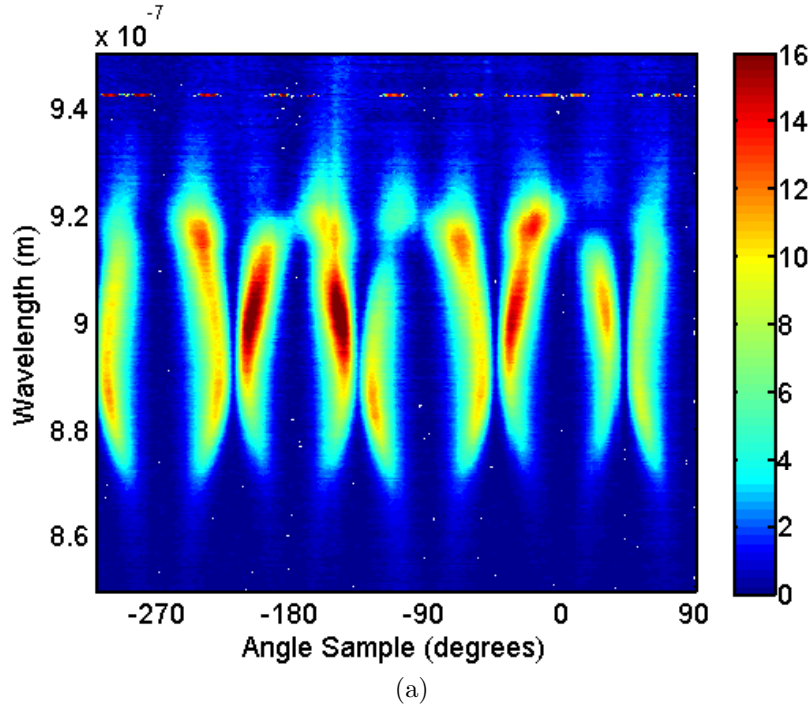
Figure 22: Panel (a) shows the reflection as a function of wavelength and angle of the sample as a false color plot. The color scale ranges from 0% to 16% reflection. For a fixed angle of incidence of 60°, we measured the reflection every three degrees. We linearly interpolated the data eight times between each angle in order to obtain a smoother plot. The incident light is p-polarized, the analyzer is set to s-polarization. Note that in this figure the interval $[-315°, -270°]$ in principle is the same measurement as $[45°, 90°]$. Panel (b) shows reflection spectra every 45°, from $-315°$ to 90°. Due to the symmetry of the system at these angles, the reflection should be 0% for every wavelength.

6 Conclusion

We performed angle-dependent optical reflection and transmission measurements on different types of GNHAs and a DNHA. Diffraction from a GNHA enables excitation of plasmon modes, resulting in an extraordinary transmission. We applied a well-known, simple model to predict the spectral position of these modes as function of angle of incidence [3]. We demonstrated that this simplified model is more accurate than previously assumed, if the dispersion of the refractive index of the metal is taken into account.

When a dielectric pillar is placed in each hole of a conventional GNHA, the transmission through the array is increased. Also, the degeneracy of modes at the pillar side of the array is lifted, both for arrays with hexagonal and square lattice symmetry. For both types of arrays a fill fraction of pillars of only 2.3% results in a remarkably large splitting of $\sim 6\%$ at normal incidence.

When the GNHA is coated with a thin layer of glass, the modes at the 'air'-side of the array shift towards longer wavelengths. Also, new types of resonances appear. This is due to the fact that the thin layer of glass acts as a dielectric waveguide. We calculated the spectral position of these new modes as a function of angle of incidence and found good agreement between this model and the measurements.

We investigated the effect of tuning the refractive index at the 'air'-side of a conventional GNHA, by placing it in liquids with different refractive indices. If the difference between the refractive index at the 'air'-side and the substrate-side is more than 3% two separate resonances, due to the excitation of SPPs at both sides of the array, can be distinguished. As the difference in refractive index is reduced the low-energy mode broadens and gains amplitude at the expense of the high-energy mode. Eventually, if the refractive indices at both sides of the array are matched, a single, broad resonance remains. The enhancement in the peak-transmission of this mode is a factor ~ 2.5, contrary to reference [26] that claimed an enhancement of an order of magnitude. We ascribe the difference to the fact that in reference [26] the size of the sample and the large numerical aperture were not taken into account.

Finally, we extended the Fano model from reference [15] to include loss and explain reflection measurements on a DNHA. The model treats the array as an optical resonator where interference occurs between a direct and an indirect channel. We demonstrated that the agreement between this model and the measurements is good, i.e. it explains all qualitative observed effects. For instance, it reveals the observed asymmetry reversal of the resonance that occurs at Brewster's angle, where the phase of the directly reflected light changes sign.

References

[1] T.F. Krauss and R.M. De La Rue, Photonic crystals in the optical regime - past, present and future, Progress in Quantum Electronics 23, 51-96 (1999)

[2] E. Yablonovitch, Photonic Crystals: Semiconductors of Light, Scientific American 47-55 (2001)

[3] T.W. Ebbesen, H.J. Lezec, H.F. Ghaemi, T. Thio and P.A. Wolff, Extraordinary optical transmission through sub-wavelength hole arrays, Nature 391, 667-669 (1998)

[4] V.N. Astratov, D.M. Whittaker, I.S. Culshaw, R.M. Stevenson, M.S. Skolnick, T.F. Krauss and R.M. De La Rue, Photonic band-structure effects in the reflectivity of periodically patterned waveguides, Phys. Rev. B., 60, 24 (1999)

[5] D.M. Whittaker, I.S. Culshaw, Scattering-matrix treatment of patterned multilayer photonic structures, Phys. Rev. B., 60, 4 (1999)

[6] D. Stolwijk, E. F. C. Driessen, M. A. Verschuuren, G. W. 't Hooft, M. P. van Exter, and M. J. A. de Dood, Enhanced coupling of plasmons in hole arrays with periodic dielectric antennas, Opt. Lett. Vol. 33, Iss. 4, pp. 363-365, (2008) (See Appendix)

[7] M.J.A. de Dood, E.F.C. Driessen, D. Stolwijk, and M.P. van Exter, Observation of coupling between surface plasmons in index-matched hole arrays, Phys. Rev. B. 77, 115437 (2008) (See Appendix)

[8] E.F.C. Driessen, D. Stolwijk and M.J.A. de Dood, Asymmetry reversal in the reflection from a 2-dimensional photonic crystal, Opt. Lett. 32, 3137 (2007) (See Appendix)

[9] Frank L. Pedrotti, S.J., Leno S. Pedrotti, Introduction to Optics, (Second edition, 1993, 1987 by Prentice-Hall, Inc.)

[10] H. A. Bethe, Theory of diffraction by small holes, Phys. Rev. 66, 163 (1944)

[11] Hermann A. Hauss, Waves and Fields in Optoelectronics, First edition, Prentice-Hall, Inc. (1984)

[12] L. Martín-Moreno, F.J. García-Vidal, H.J. Lezec, K.M. Pellerin, T. Thio, J.B. Pendry and T.W. Ebbesen, Theory of Extraordinary Optical Transmission through Subwavelength Hole Arrays, Phys. Rev. Let., 86, 6 (2001)

[13] H. Raether, Surface Plasmons on Smooth and Rough Surfaces and on Gratings, Springer-Verlag Berlin Heidelberg (1988)

[14] http://ab-initio.mit.edu/wiki/index.php/MIT_Photonic_Bands

[15] S. Fan, W. Suh and J.D. Joannopoulos, Temporal coupled-mode theory for the Fano resonance in optical resonators, Opt. Soc. Am. A. Vol. 20, No. 3, 569-572, (2003)

[16] U. Fano, Effects of Configuration Interaction on Intensities and Phase Shifts, Phys. Rev. 124, 1866 (1961)

[17] M. Born and E. Wolf, Principles of Optics (Pergamon, Oxford, 1980)

[18] E.D. Palik, Handbook of Optical Constants of Solids I (Academic Press, SanDiego, 1985)

[19] Conventional refers to being similar to the ones most widely used in literature [3].

[20] E. Altewischer, Subwavelength hole arrays, surface plasmons and quantum entanglement (proefschrift chapter 2)

[21] C. Genet, M.P. van Exter, J.P. Woerdman, Fano-type interpretation of red shifts and red tails in hole array transmission spectra, Opt. Com. 225 (2003) 331-336

[22] K.L. van der Molen, F.B. Segerink, N.F. van Hulst and L. Kuipers, Influence of hole size on the extraordinary transmission through subwavelength hole arrays, Appl. Phys. Lett. 85, 4316-4318 (2004)

[23] A. Adams, J. Moreland, P.K. Hansma and Z. Schlesinger, Light emission from surface-plasmon and waveguide modes excited by N atoms near a silver grating, Phys. Rev. B. 25, 3457 - 3461 (1982)

[24] M. J. A. de Dood, E. F. C. Driessen, D. Stolwijk, M. P. van Exter, M. A. Verschuuren, G. W. 't Hooft, Index matching of surface plasmons, Proc. SPIE, Vol. 6987, 698713 (2008)

[25] http://www.wiredchemist.com/chemistry/data/

physical_character_solvents.html

[26] A. Krishnan, T. Thio, T.J. Kim, H.J. Lezec, T.W. Ebbesen, P.A. Wolff, J. Pendry, L. Martin-Moreno, F.J. Garcia-Vidal, Evanescently coupled resonance in surface plasmon enhanced transmission, Opt. Com., 200, 1-7 (2001)

[27] E. Hecht, Optics, third edition, Addison-Wesley (1998)

[28] H.P. Urbach and G.L.J.A. Rikken, Spontaneous emission from a dielectric slab, Phys. Rev. A., 57, 5 (1998)

[29] J. C. Maxwell-Garnett, Colours in Metal Glasses and in Metallic Films, Philos. Trans. R. Soc. London A203, 385 (1904)

[30] A. Kirchner, K. Busch, and C.M. Soukoulis, Transport properties of random arrays of dielectric cylinders, Phys. Rev. B., 57, 1 (1998)

7 Acknowledgement

I would like to thank the following people:

- Michiel de Dood for his stimulating supervision and his patience (especially with regard to my report).

- Eduard Driessen for his supervision and the many discussions, especially about the research presented in chapter 5.

- Martin van Exter and Gert 't Hooft for their contributions to chapter 4.

8 Appendix: List of Publications

The work in this thesis has contributed to three publications:

- D. Stolwijk, E. F. C. Driessen, M. A. Verschuuren, G. W. 't Hooft, M. P. van Exter, and M. J. A. de Dood, Enhanced coupling of plasmons in hole arrays with periodic dielectric antennas, Opt. Lett. Vol. 33, Iss. 4, pp. 363-365, (2008) (section 4.2)

- M.J.A. de Dood, E.F.C. Driessen, D. Stolwijk, and M.P. van Exter, Observation of coupling between surface plasmons in index-matched hole arrays, Phys. Rev. B. 77, 115437 (2008) (section 4.4)

- E.F.C. Driessen, D. Stolwijk and M.J.A. de Dood, Asymmetry reversal in the reflection from a 2-dimensional photonic crystal, Opt. Lett. 32, 3137 (2007) (chapter 5)

The work from chapter 4 has been presented on a poster at the physics@FOM conference in Veldhoven, The Netherlands, January 2008.

Enhanced coupling of plasmons in hole arrays with periodic dielectric antennas

D. Stolwijk,[1] E. F. C. Driessen,[1] M. A. Verschuuren,[2] G. W. 't Hooft,[1,2] M. P. van Exter,[1] and M. J. A. de Dood[1,*]

[1]*Huygens Laboratory, Leiden University, P.O. Box 9504, 2300 RA Leiden, The Netherlands*
[2]*Photonic Materials and Devices, Philips Research, High Tech Campus 4 (mailstop 12), 5656 AE Eindhoven,
The Netherlands*
*Corresponding author: mdedood@molphys.leidenuniv.nl

We compare the angle-dependent transmission spectra of a metal hole array with dielectric pillars in each hole with that of a conventional metal hole array. The pillars enhance the optical transmission as well as the interaction between surface plasmon modes. This results in an observed splitting $\Delta\omega/\omega$ as large as 6%, at normal incidence, for the modes on the pillar side of the array. © 2008 Optical Society of America

OCIS codes: 240.6680, 290.0290, 230.5298.

Metal films perforated with an array of subwavelength holes have intrigued researchers since the discovery that these arrays show extraordinary transmission [1]. It is generally accepted that the enhanced transmission is mediated by surface plasmons, i.e., electromagnetic surface waves that are bound to a metal-dielectric interface. On a smooth interface these waves cannot be excited directly because their momentum is larger than that of light incident from the dielectric. Diffraction from a regular array of holes enables efficient excitation of the plasmon modes and increases the transmission.

The transmission spectra of metal hole arrays show a number of asymmetric resonances that correspond to different diffraction orders. Each resonance can be labeled by a specific reciprocal lattice vector [2]. The asymmetric line shape of the resonances can be explained in terms of a phenomenological (Fano) model [3–5]. Each peak features a maximum in transmission and a profound minimum, known as Wood's anomaly [6]. The frequencies of these features depend on the angle of incidence and can be compared to the dispersion relation of a plasmon on a smooth surface folded back to the first Brillouin zone of the periodic lattice [2].

In this Letter we study the *p*-polarized transmission spectra of metal films perforated with a square lattice of subwavelength holes. We compare the transmission of an array with a dielectric pillar in each of the holes with that of a conventional hole array. Transmission spectra of conventional hole arrays have been studied previously [7,8] and show that different modes can be excited depending on the input polarization. The *p*-polarized input light dominantly excites plasmon modes, which propagate in the direction parallel and antiparallel to the projected wave vector of the incident light. For small angles of incidence, coupling to modes that propagate in the approximately orthogonal direction is inefficient. We show that the excitation of these modes is strongly enhanced for the hole array with pillars. The pillars in the holes act as antennas that enhance the coupling to these modes. This provides a way of controlling the interaction between light and surface plasmon modes.

The metal hole arrays in the experiment were made using an imprinting technique. An array of pillars was defined by electron-beam lithography and was used to create a rubber stamp. A replica of the array was created by pressing the stamp into a layer of liquid sol–gel glass. This second array is then coated with a layer of gold. The gold was selectively removed from the pillars by making use of the fact that the gold layer deposited on the side of the pillars is thinner than the layer on the substrate. The result is a metal hole array with an ~650 nm long glass pillar sticking out of each hole as shown in Fig. 1. The 0.5 mm × 0.5 mm array was created on an AF45 glass substrate with $n \approx 1.52$. A 100 nm thick layer of sol–gel glass with a refractive index $n \approx 1.41$ was left between the substrate and the gold layer. The gold layer is 200 nm thick and is perforated by a square array of pillars with a lattice constant $a = 760 \pm 4$ nm [9] and a diameter $d = 135 \pm 5$ nm. After measuring the transmission of this array, we selectively removed the pillars using hydrofluoric acid and repeated the transmission measurement.
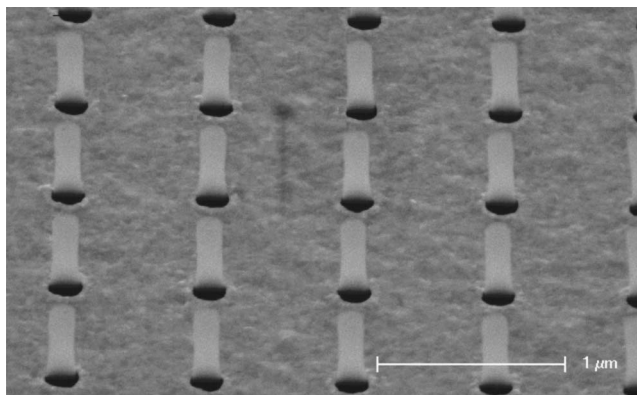

Fig. 1. Scanning electron microscope image of the metal hole array created using an imprinting technique. The holes are 132 nm in diameter and each hole contains an ~650 nm high glass pillar. The array has a lattice constant $a = 760$ nm.

The optical transmission of the hole array was measured using an incandescent lamp coupled to a 200 μm multimode fiber. A set of lenses was used to create an ~300 μm diameter spot on the sample. The transmitted light was sent to a fiber-coupled grating spectrometer with a CCD detector (resolution 1.2 nm) to measure the spectral content. The numerical aperture of the incident and transmitted light beam was limited to <0.01. Polarizers were placed in parallel parts of the incident and transmitted beams. The substrate was placed onto a rotation mount with the rotation axis aligned with the (0, 1) direction of the hole array. The wave vector of the incident light was perpendicular to this direction.

Figure 2 shows measured transmission spectra (normalized to the lamp spectrum) of the metal hole array both before (dashed curves) and after (solid curves) removing the pillars. Spectra are shown for normal incidence (bottom) and a 15° angle of incidence (top). The maximum transmission, shown in Fig. 2, decreases and at the same time the resonance narrows, while the maximum shifts to shorter wavelengths. The observed change in line shape corresponds to a Fano resonance for which the amplitudes of both the direct and resonant channels as well as the linewidth of the resonance are reduced by a factor of 2. Note that the spectral positions of the transmission minima do not shift when the hole size is reduced [6,10]. The marginal shift that we do observe is attributed to the fact that the pillars change the effective index of the surface plasmon.

Each resonance in the transmission spectra can be labeled by a specific choice of a reciprocal lattice vec-

tor. The labels (i,j) in Fig. 2 refer to the reciprocal lattice vector $\vec{G} = i\vec{G}_x + j\vec{G}_y$, where $\vec{G}_{x,y}$ are the two basis vectors of the reciprocal lattice. The condition for exciting a surface plasmon mode is given by

$$\vec{k}_\parallel = \vec{k}_{SP} + \vec{G}, \tag{1}$$

where $\vec{k}_\parallel$ is the projection of the wave vector of the incoming light onto the metal-dielectric interface and $\vec{k}_{SP}$ is the wave vector of the surface plasmon. To describe the dispersion, we approximate the wave vectors of the surface plasmons on both sides of the metal hole array with that of a plasmon on a smooth metal-dielectric interface

$$k_{SP}(\omega) = \frac{\omega}{c} \left(\frac{\varepsilon_d \varepsilon_m(\omega)}{\varepsilon_d + \varepsilon_m(\omega)} \right)^{1/2}, \tag{2}$$

where c is the speed of light, ε_d is the dielectric constant of the dielectric, and $\varepsilon_m(\omega)$ is the frequency dependent dielectric constant of the metal.

Figure 3 shows gray scale plots of the transmission as a function of the angle of incidence (horizontal axis) and the wavelength (vertical axis) for the sample without pillars (top) and with pillars (bot-
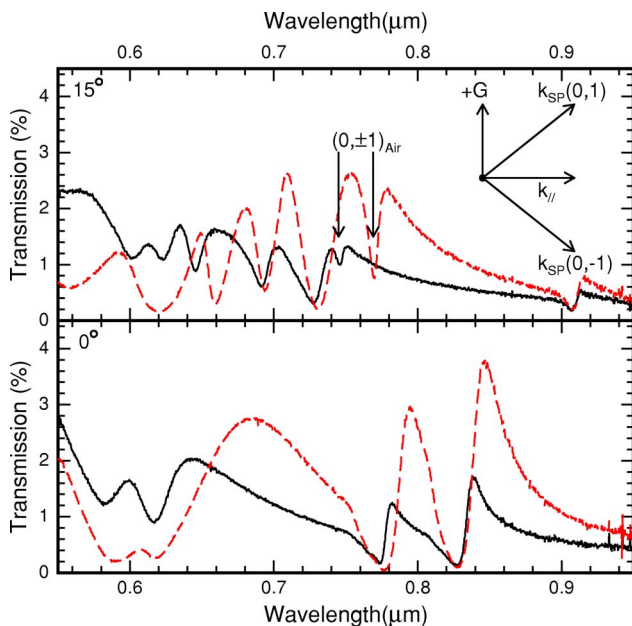

Fig. 2. (Color online) Transmission spectra for p-polarized light of a conventional metal hole array (solid curve) and a metal hole array with pillars (dashed curve). Spectra are shown for normal incidence (bottom) and 15° angle of incidence (top). The arrows indicate the $(0, \pm 1)$ resonance for a 15° angle of incidence. The inset shows the wave vector $\vec{k}_\parallel$, a reciprocal lattice vector $\vec{G}$ in the (0,1) direction and the propagation direction of the two $(0, \pm 1)$ modes.
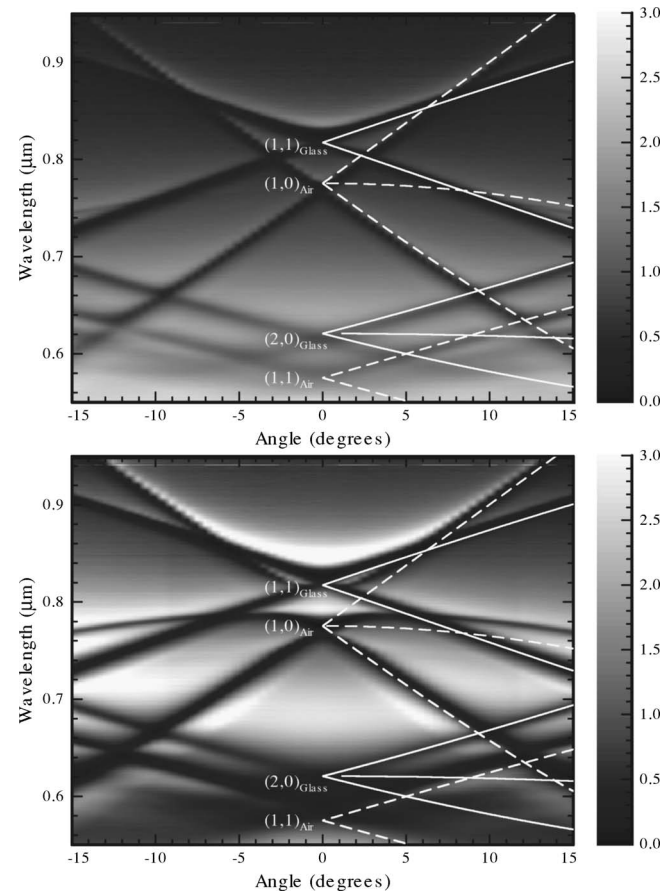

Fig. 3. Gray scale plots of the measured transmission as a function of angle of incidence and wavelength for the metal hole array without pillars (top) and with pillars (bottom). The gray scale ranges from 0% to 3% transmission. The lines indicate the frequencies calculated from Eqs. (1) and (2). The solid lines are for modes on the glass side, while the dashed lines are for modes on the air side.

tom). The dark bands in the figure correspond to the minima in the transmission spectra. The white lines are calculated from Eqs. (1) and (2) for different reciprocal lattice vectors $\vec{G}$ using the frequency dependent dielectric constant of gold [11] and an effective index of $n \approx 1.46$ for the glass substrate [12]. A distinction is made between the surface plasmon modes on the air side (dashed lines) and on the glass side (solid lines). The $(\pm 1,0)$ and $(0,\pm 1)$ modes on the air side are degenerate at normal incidence. When the angle of incidence is changed, the degeneracy is lifted, and the resonance splits into a $(1,0)$, a $(-1,0)$, and a degenerate $(0,\pm 1)$ resonance. The $(1,0)$ and $(-1,0)$ modes have a strong dispersion, because $\vec{k}_\parallel$ and $\vec{G}$ are parallel. For the $(0,\pm 1)$ modes the dispersion calculated from Eq. (1) is limited, corresponding to the fact that $\vec{k}_\parallel$ and $\vec{G}$ are perpendicular. For the conventional array the $(0,\pm 1)$ resonance is barely visible for small angles, consistent with earlier work [8]. The resonance is strikingly visible in the transmission of the array with pillars. The large difference in amplitude for this resonance is also clearly visible in the top part of Fig. 2 (arrows).

In our geometry, the scattering plane coincides with a $(1,0)$ direction of the square lattice. This plane is a mirror plane of the hole array, and the modes can be classified as either odd or even relative to this plane. Relative to this plane, the p-polarized input light has an odd H-field distribution, and only plasmon modes with an odd H-field distribution can be excited. At normal incidence, this corresponds to plasmon modes that propagate in the direction of the E-field vector [13], i.e., the $(\pm 1,0)$ directions. For nonzero angles of incidence it is possible to couple to a combination of $(0,\pm 1)$ modes. The direction of propagation of these modes is sketched in the inset of Fig. 2. The pillars in the holes do not change the symmetry. They act as antennas and affect the efficiency with which the modes are excited. The interaction between light and a dielectric pillar is strongest when the E-field is parallel to the long axis of the pillars. As a result, the coupling to the $(0,\pm 1)$ modes on the air side is enhanced for p-polarized light.

For both arrays, the angle dependent transmission in Fig. 3 shows that the $(\pm 1,0)$ air modes have an almost linear dispersion at sufficiently large angles of incidence. For smaller angles, this only holds for the conventional hole array. For the hole array with pillars the $(\pm 1,0)$ modes on the air side are clearly coupled. At normal incidence we observe two minima in the spectra at 775 and 825 nm. The minimum at 825 nm coincides with the minimum of the $(1,1)$ glass modes. At normal incidence, the excited plasmon modes are standing waves. The resonances occur at different energies depending on the position of the nodes and antinodes of the standing waves relative to the holes [4,14]. Without pillars, this energy difference is small and the splitting is not resolved. The pillars only lower the energy of the mode that has antinodes at the position of the pillars. For our array, with a fill fraction of pillars of only 2.3%, this leads to

an observed splitting of the resonances of 6% of the center frequency. Note that we used the separation between the minima as a measure of the splitting, because the minima do not shift when radiation losses are increased [6,10]. We have compared this splitting to a two-band model and to a model that uses the polarizability per unit volume. The splitting calculated from these simplified models is much smaller than the observed splitting.

Increasing the fill fraction of pillars will certainly increase the energy difference between the modes. However, a larger hole size also leads to larger radiation losses [4] and broadens the spectral features. This may obscure the effect. Similar effects can be realized when dielectric hole arrays are placed on top of a metal hole array, although the interaction with p-polarized light is generally weaker for holes when compared to pillars. These hybrid structures can be used to (locally) tune the dispersion of the surface modes of a metal film. By locally adding or removing pillars (holes), control of the excitation and propagation of plasmons on a wavelength scale can be achieved. When the interaction between plasmon modes can be increased, it becomes conceivable that two-dimensional periodic metal-dielectric structures exist that do not allow coupling of light waves to surface modes in any direction for a certain range of frequencies. This effect would be analogous to the existence of photonic bandgaps in two-dimensional dielectric structures.

References and Notes

1. T. W. Ebbesen, H. J. Lezec, H. F. Ghaemi, T. Thio, and P. A. Wolff, Nature **391**, 667 (1998).
2. H. F. Ghaemi, T. Thio, D. E. Grupp, T. W. Ebbesen, and H. J. Lezec, Phys. Rev. B **58**, 6779 (1998).
3. U. Fano, J. Opt. Soc. Am. **31**, 213 (1941).
4. C. Ropers, D. J. Park, G. Stibenz, G. Steinmeyer, J. Kim, D. S. Kim, and C. Lienau, Phys. Rev. Lett. **94**, 113901 (2005).
5. C. Genet, M. P. van Exter, and J. P. Woerdman, J. Opt. Soc. Am. A **22**, 998 (2005).
6. R. W. Wood, Phys. Rev. **48**, 928 (1935).
7. E. Altewischer, M. P. van Exter, and J. P. Woerdman, J. Opt. Soc. Am. B **20**, 1927 (2003).
8. W. L. Barnes, W. A. Murray, J. Dintinger, E. Devaux, and T. W. Ebbesen, Phys. Rev. Lett. **92**, 107401 (2004).
9. The lattice constant was obtained from diffraction measurements with an He–Ne laser.
10. K. L. van der Molen, K. J. Klein Koerkamp, S. Enoch, F. B. Segerink, N. F. van Hulst, and L. Kuipers, Phys. Rev. B **72**, 045421 (2005).
11. P. B. Johnson and R. W. Christy, Phys. Rev. B **6**, 4370 (1972).
12. The effective index is based on the calculated surface plasmon of gold with a 100 nm layer of sol–gel glass.
13. S. C. Hohng, Y. C. Yoon, D. S. Kim, V. Malyarchuk, R. Müller, Ch. Lienau, J. W. Park, K. H. Yoo, J. Kim, H. Y. Ryu, and Q. H. Park, Appl. Phys. Lett. **81**, 3239 (2002).
14. W. L. Barnes, T. W. Preist, S. C. Kitson, and J. R. Sambles, Phys. Rev. B **54**, 6227 (1996).

Observation of coupling between surface plasmons in index-matched hole arrays

Michiel J. A. de Dood, Eduard F. C. Driessen, Daniël Stolwijk, and Martin P. van Exter

Huygens Laboratory, P.O. Box 9504, 2300 RA Leiden, The Netherlands

We measured the transmission of a large array of holes in an optically thick gold film, immersed in liquids of different refractive indices. For a large difference in refractive index between the substrate and the liquid ($\Delta n \gtrsim 0.05$), the transmission spectra contain separate resonances, due to surface plasmons propagating on each of the metal-to-dielectric interfaces. When the index difference is reduced we observe an avoided crossing between a strong low-energy mode and a weak high-energy mode. The low-energy mode becomes broader and gains amplitude at the expense of the high-energy mode. For an index-matched array, a single broad resonance remains. These observations provide direct evidence that the two surface plasmon modes on both sides of the interface are coupled.

PACS number(s): 73.20.Mf, 42.25.Fx, 78.66.Bz, 41.20.Jb

The observation of enhanced transmission of light through a periodic array of subwavelength holes in an optically thick metal film[1] triggered interest in the coupling between light and surface plasmons. This coupling occurs via diffraction of the periodic lattice, effectively adding a reciprocal lattice vector to the wave vector of the incoming light. The diffraction enables efficient excitation of a surface plasmon mode on one of the metal-to-dielectric interfaces. Due to this excitation, the transmission of the hole array exceeds that what is expected based on diffraction from a set of independent single holes.[2]

It is well known that coupling of different surface plasmon modes on the same interface, via Bragg scattering, leads to the formation of bright and dark modes in one-dimensional arrays of slits or wires.[3–5] Alternatively, plasmons on a single interface can be coupled to a waveguide mode.[6,7] The coupling between plasmons on different interfaces is more difficult to observe, because in most cases the plasmon resonances on different sides of the metal film are detuned in frequency. This is due to the inherent asymmetry of a metal film on a substrate. This asymmetry can be removed by either fabricating a symmetric sample or by using index matching liquids.[8–10] The observed transmission spectra generally resemble the calculated spectra,[9,11] but the finite size of the arrays and the numerical aperture of the incoming beam limit a proper observation of the coupling between the modes.

Here, we present transmission measurements on a large two-dimensional metal hole array, using a white light beam with a numerical aperture that is small enough to resolve the coupled modes. We obtain the frequency, the linewidth, and the amplitude of the resonances by fitting the transmission spectra to multiple Fano resonances.[5,12] When the index difference between substrate and liquid is reduced we observe an avoided crossing between a broad low-energy mode and a narrow high-energy mode. At the same time the linewidth and the amplitude of the low-energy mode increase at the expense of the high-energy mode. These modes correspond to the two peaks in the transmission spectrum that can be identified as surface plasmons propagating on either the substrate or the liquid side of the metal film. Our observations

can be described by coupled-mode theory and are consistent with calculations[9,11] that use tunneling of light through the holes as the coupling mechanism.

In our experiments, a metal hole array on a glass substrate was mounted inside a closed glass cuvette with a 2.5 mm optical path length. The array was immersed in different refractive index solutions: we used mixtures of ethanol and benzyl alcohol to cover the range $n = 1.36 – 1.54$ and mixtures of benzyl alcohol and bromonaphtalene for the range $n = 1.54 – 1.66$. The refractive index of each mixture was determined by Abbe refractometry and is close to the volume average of the refractive index of the two liquids. The glass substrate (Schott-BK7) has a nearly constant refractive index $n = 1.51$ over the wavelength range of interest. The metal hole array is a large (1×1 mm^2) square array of 200 nm diameter holes with a lattice constant $a = 700$ nm in an optically thick (200 nm) gold film. A 2 nm thick Ti bonding layer ensures proper adhesion of the gold layer. The optical transmission was measured at normal incidence. We used a fiber-coupled lamp to illuminate an ~ 300 μm diameter spot on the sample, thus avoiding edge effects. The transmitted light was sent to a fiber-coupled grating spectrometer with a Si charge-coupled device array (resolution 1.2 nm, 550 – 1000 nm) or an InGaAs linear array (resolution 3.0 nm, 900 – 1700 nm). Apertures in the incident and transmitted light beam were used to limit the numerical aperture (NA) below 0.01.

Figure 1 shows the measured transmission as function of frequency. Spectra are shown for the metal hole array in air (solid line), and immersed in a liquid with refractive index $n_L = 1.50$ (dashed line). The spectra show a number of resonant peaks for which the transmission is enhanced. This is a result of coupling of incident radiation to surface plasmons that propagate on either the metal-to-air or metal-to-substrate interface. The condition for coupling to such a surface plasmon is given by $\mathbf{k}_\parallel = \mathbf{k}_{SP} + \mathbf{G}$, where $\mathbf{k}_\parallel$ is the component of the wave vector of the incident light along the interface, $\mathbf{k}_{SP}$ is the wave vector of the surface plasmon, and $\mathbf{G}$ is a reciprocal lattice vector. For normal incidence this condition leads to a set of resonance frequencies given by
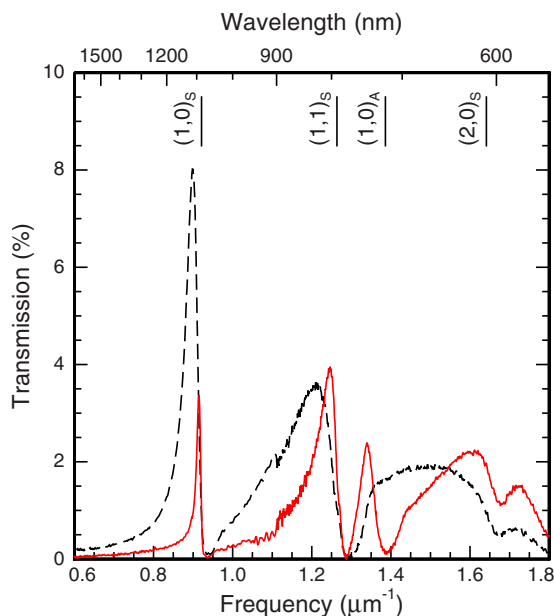
FIG. 1. (Color online) Transmission as function of frequency for a metal hole array in air (solid line, $n_L = 1.00$) and nearly index matched (dashed line, $n_L = 1.50$). The vertical lines indicate the calculated spectral positions of the different plasmon resonances on the substrate (S) and air (A) side of the array for $n_L = 1.00$.

$$\omega_{res} = \frac{|\mathbf{G}|c}{n} \sqrt{1 + \frac{n^2}{\epsilon_m(\omega)}}, \qquad (1)$$

where c is the speed of light in vacuum, n is the refractive index of the dielectric, and $\epsilon_m(\omega)$ is the frequency-dependent dielectric constant of the metal. For a square lattice, the length of the reciprocal lattice vector is $|\mathbf{G}| = \sqrt{(N_x^2 + N_y^2)} 2\pi/a$, with N_x and N_y integers. Therefore, the resonances can be labeled as $(N_x, N_y)_{S,A}$, where the subscript indicates whether the resonance occurs on the substrate (S) or on the air (A) side of the metal hole array. To calculate the resonance frequencies we use literature values of the dielectric constant of gold[13] and take the dielectric constants of air and glass as constant. The vertical lines in Fig. 1 indicate the calculated positions of the different resonances. For an asymmetric structure with air on one side and glass on the other side, the resonances from the two sides are well separated.

When the air is replaced by a nearly index-matching liquid, the transmission spectrum changes drastically (see the dashed line in Fig. 1). The $(1,0)_A$ mode on the metal-to-liquid interface shifts in frequency from 1.387 μm^{-1} (721 nm) to 0.922 μm^{-1} (1085 nm) to coincide with the $(1,0)_S$ mode on the metal-to-substrate interface. The peak transmission of the combined (1,0) mode is roughly a factor of 2 higher, and a significant broadening of the resonance is observed.

The frequencies of the maxima in the transmission spectra are plotted in Fig. 2 as a function of the refractive index of the liquid (symbols). The dashed lines are the frequencies of the different modes as predicted by Eq. (1). The modes can be classified in two categories: modes on the metal-to-
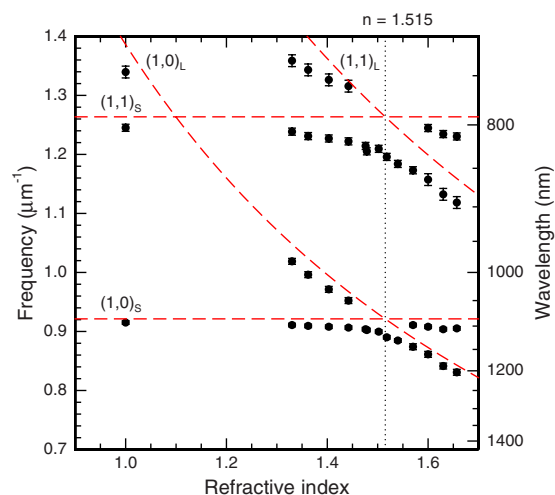

FIG. 2. (Color online) Frequencies of the maximum in transmission as function of refractive index obtained directly from the transmission data. The dashed lines show the calculated resonance frequencies according to Eq. (1).

substrate interface (labeled "S"), which do not shift when the index of the liquid is changed, and modes on the metal-to-liquid interface (labeled "L"), which show a strong redshift in frequency when the refractive index of the liquid is increased. To correctly predict the resonance frequencies from Eq. (1) the frequency-dependent dielectric constant of the metal should be included. The index dispersion of the liquids and the glass can be neglected.

The transmission through a metal hole array can be described as a combination of a nonresonant direct transmission through the holes, and a resonant component that couples to surface plasmons.[5,11,12,14,15] Interference between these two contributions gives an asymmetric line shape. The transmission spectra $T(\omega) = |t(\omega)|^2$ can be expressed as a sum over a finite number of (uncoupled) resonances

$$t(\omega) = a_{nr}\omega^2 + \sum_j \frac{b_j \Gamma_j \exp(i\varphi_j)}{(\omega - \omega_j) + i(\Gamma_j + \gamma_j)}, \qquad (2)$$

where Γ_j is the radiative loss and γ_j is the intrinsic Ohmic loss of mode j. The resonance at frequency ω_j has an amplitude b_j and a phase φ_j. The slowly varying nonresonant contribution has an amplitude a_{nr} and is proportional to ω^2 to reflect the fact that the transmitted intensity is proportional to ω^4 for a single subwavelength hole in a thin film of a perfect conductor.[2] In the limit of long wavelengths the dielectric constant of the metal approaches that of the perfect conductor, while the film thickness relative to the wavelength becomes negligible and Eq. (2) gives the correct result. In principle, Eq. (2) allows a separation of resonant and nonresonant contributions, but in practice the number of separate resonances that can be identified in measured transmission spectra is limited. This complicates the interpretation of a_{nr} because the nonresonant term now also contains a contribution from resonances at higher frequencies.

Figure 3 shows the frequency of the peaks as a function of the refractive index in more detail (a), and corresponding
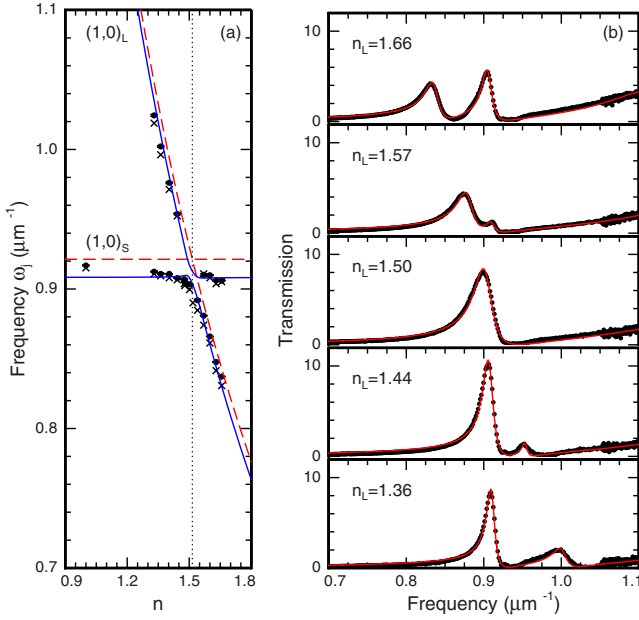
FIG. 3. (Color online) Detail of the crossing between the (1,0) modes (a) and corresponding spectra (b). The crosses are the peak frequencies obtained directly from the measured data, while closed symbols are the frequencies ω_j from fitting the transmission data to four Fano resonances. The solid lines are a fit to coupled-mode theory (see text). The measured transmission (b) is shown for different refractive indices of the liquid (dots) and can be fitted to the Fano expression (lines).
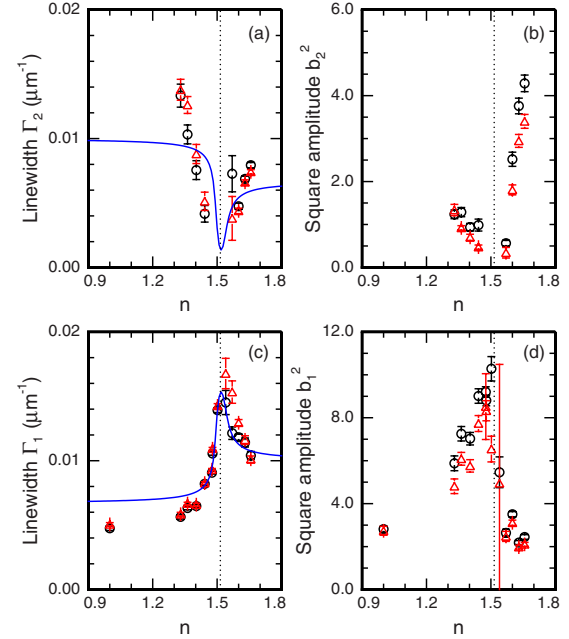

FIG. 4. (Color online) Linewidth Γ and square amplitude b^2 for the lowest two resonances as function of refractive index. The low-frequency mode [(c) and (d)] is always present and both linewidth and amplitude show a maximum around the index-matched situation ($n_L=1.515$, dotted line). At the same time, the second mode shows a minimum in linewidth and amplitude and disappears from the spectra for nearly index-matched samples. The solid line is a fit to coupled-mode theory (see text).

transmission measurements in the frequency range between 0.7 and 1.1 μm^{-1} (b). The solid lines are fits to Eq. (2), containing up to four resonant contributions. In these fits, the Ohmic losses γ_j were set to zero.[16] This description is valid for the typical situation that the radiative loss is much larger than the intrinsic Ohmic loss. The number of fit parameters can be reduced by setting all phases φ_j equal to π. This corresponds to the normal situation, where the resonant channel is out of phase with the direct channel. This choice does not affect the values of the other fit parameters significantly.

The crosses in Fig. 3(a) refer to the frequencies of the transmission maxima determined directly from the experimental data. These maxima are close to the resonance frequencies obtained from the fits (solid symbols). When the refractive index of the liquid is close to that of the substrate, the transmission spectrum is reduced to a single peak. Two distinct peaks can be observed for an index difference between liquid and substrate larger than $\sim$0.05. In addition, the linewidth and amplitude of the resonances depend strongly on the refractive index. The low-frequency resonance broadens and grows in amplitude when the refractive index is increased, while the high-frequency resonance narrows and diminishes in amplitude.

Figure 4 shows the linewidth Γ_j and square amplitude b_j^2 obtained from the fit of Eq. (2) to the transmission data. The triangular symbols refer to a fit where all parameters were kept free, while the circular symbols refer to a fit with all phases φ_j equal to π. The data in Fig. 4 confirm that the

low-frequency mode (mode 1) gains amplitude and broadens while the high-frequency mode (mode 2) is reduced in amplitude and narrows. Note that a typical value of $\Gamma=0.01$ μm^{-1} corresponds to a propagation distance $x=1/(2\pi\Gamma)\approx16$ μm. This is much smaller than the illuminated spot size (300 μm) and the coherence length $D\sim\lambda/NA$, which we estimate 100 μm for a NA of less than 0.01. The avoided crossing together with the data in Fig. 4 prove that the two surface plasmons on different sides of the optically thick metal film are coupled.

A coupled-mode theory with only two modes is sufficient to describe our data. These modes correspond to the two surface plasmons that propagate on either the substrate or the liquid side of the metal film. In this analysis, we treat the plasmon modes on the same interface that are coupled via Bragg reflection[3–5] as a single mode. The time evolution of the amplitudes a and b of the two modes in our model is given by the equation of motion

$$i\frac{\mathrm{d}}{\mathrm{d}t}\begin{pmatrix} a \\ b \end{pmatrix} = H\begin{pmatrix} a \\ b \end{pmatrix}. \quad (3)$$

The Hamiltonian H that describes the coupled system has the following form:

$$H = \begin{pmatrix} \omega_a + V - i\Gamma_a & W + i\Gamma_C \\ W + i\Gamma_C & \omega_b + V - i\Gamma_b \end{pmatrix}. \quad (4)$$

The diagonal elements of the matrix contain the frequencies $\omega_{a,b}$ and linewidths $\Gamma_{a,b}$ of the uncoupled modes, and a fre-

TABLE I. Fit parameters of the coupled-mode theory described in the text.

V : Frequency shift	$-0.013 \pm 0.028 \ \mu m^{-1}$
Γ_a : Damping rate of mode a	$0.0067 \pm 0.0004 \ \mu m^{-1}$
Γ_b : Damping rate of mode b	$0.0100 \pm 0.0005 \ \mu m^{-1}$
W : Conservative coupling rate	$0.0046 \pm 0.0015 \ \mu m^{-1}$
Γ_C : Dissipative coupling rate	$0.0068 \pm 0.0011 \ \mu m^{-1}$

quency shift V. The off-diagonal elements contain parameters W and Γ_C that describe conservative coupling (leading to mode splitting and an avoided crossing), and dissipative coupling (leading to mode pulling or frequency locking), respectively.[17,18] The complex eigenvalues of the Hamiltonian H give the frequencies $\omega_{1,2}$ and linewidths $\Gamma_{1,2}$ of the coupled modes.

The solid lines in Figs. 3(a) and 4 are a fit of the model to the experimental data.[19] The fit parameters are summarized in Table I. There is a small frequency redshift V, compared to the resonance frequencies predicted by Eq. (1) consistent with the theory in Ref. 11. The conservative coupling rate W causes the avoided crossing in Fig. 3(a). The frequencies ω_j can be fitted satisfactorily by setting the dissipative coupling rate Γ_C to zero. However, a system with only conservative coupling gives linewidths $\Gamma_{1,2}$ that are independent of refractive index. This is inconsistent with the data in Fig. 4. To describe the fact that the damping of one mode increases while the damping of the other mode decreases, a dissipative component in the coupling is needed. Conservative coupling is still important because a model with only dissipative coupling ($W=0$) gives significant mode pulling which is not observed in Fig. 3.

As a refinement of our model, we have also used damping rates $\Gamma_{a,b}$ that depend on the refractive index of the liquid via the optical density of states.[5,20,21] Introducing these extra fit parameters indeed results in a better fit. However, it does not affect the values of the fit parameters V, W, and Γ_C significantly, and thus does not change our interpretation of the measurements. The fit parameters in Table I indicate that the mode on the liquid side is somewhat more lossy than the mode on the glass side. It is reasonable to assume that this is

due to the fact that the roughness of the metal-to-liquid interface is larger than the interface between the metal and the polished glass substrate. From atomic force microscopy measurements on the sample we indeed find roughness (root mean square) values of 4.4 nm for the gold surface and 0.8 nm for the glass surface. In addition, some particles from the fabrication process are present on the gold-air interface adding to the scattering of surface plasmons on this interface.

The modes in our coupled-mode theory are consistent with the states calculated using a scattering formalism.[9,11] On resonance, the eigenmodes correspond to a situation where the plasmons on the two interfaces oscillate in phase (low-frequency mode) or out of phase (high-frequency mode). Close to resonance, the calculated spectra show a split resonance (avoided crossing) and a linewidth of the low-energy mode that becomes larger, while the linewidth of the high-energy mode becomes smaller. Without absorption the amplitude of the modes is equal. If absorption is included, the amplitude of the peaks is reduced depending on the linewidth (resonance time) of the mode.[9] This explains the dependence of the squared amplitude $b_{1,2}^2$ of the modes as function of refractive index given in Fig. 4.

In conclusion, we have performed index-matching experiments on large metal-hole arrays. Two plasmon modes, on different sides of the metal film, can be identified if there is a large mismatch in refractive index. The resonance in the transmission spectra is reduced to a single broad resonance when the sample is index matched. This behavior can be explained by a coupling between the two surface plasmon modes through the hole array. A coupled-mode analysis shows that the modes have an avoided crossing and correctly predicts the change in linewidth of the coupled modes when the refractive index is changed.

[1] T. W. Ebbesen, H. J. Lezec, H. F. Ghaemi, T. Thio, and P. A. Wolff, Nature (London) **391**, 667 (1998).

[2] H. A. Bethe, Phys. Rev. **66**, 163 (1944).

[3] Y. J. Chen, E. S. Koteles, R. J. Seymour, G. J. Sonek, and J. M. Ballantyne, Solid State Commun. **46**, 95 (1983).

[4] H. Lochbihler, Phys. Rev. B **50**, 4795 (1994).

[5] C. Ropers, D. J. Park, G. Stibenz, G. Steinmeyer, J. Kim, D. S. Kim, and C. Lienau, Phys. Rev. Lett. **94**, 113901 (2005).

[6] A. Christ, S. G. Tikhodeev, N. A. Gippius, J. Kuhl, and H. Giessen, Phys. Rev. Lett. **91**, 183901 (2003).

[7] T. Zentgraf, A. Christ, J. Kuhl, and H. Giessen, Phys. Rev. Lett. **93**, 243901 (2004).

[8] A. Krishnan, T. Thio, T. J. Kim, H. J. Lezec, T. W. Ebbesen, P. A.

Wolff, J. Pendry, L. Martín-Moreno, and F. J. García-Vidal, Opt. Commun. **200**, 1 (2001).

[9] L. Martín-Moreno, F. J. García-Vidal, H. J. Lezec, K. M. Pellerin, T. Thio, J. B. Pendry, and T. W. Ebbesen, Phys. Rev. Lett. **86**, 1114 (2001).

[10] L. Pang, K. A. Tetz, and Y. Fainman, Appl. Phys. Lett. **90**, 111103 (2007).

[11] F. J. Garcia de Abajo, Rev. Mod. Phys. **79**, 1267 (2007).

[12] U. Fano, J. Opt. Soc. Am. **31**, 213 (1941).

[13] P. B. Johnson and R. W. Christy, Phys. Rev. B **6**, 4370 (1972).

[14] C. Genet, M. P. van Exter, and J. P. Woerdman, Opt. Commun. **225**, 331 (2003).

[15] M. Sarrazin, J. P. Vigneron, and J. M. Vigoureux, Phys. Rev. B

67, 085415 (2003).

[16] The parameters b_j, Γ_j, and γ_j are not independent and cannot be determined by a fit of the data to Eq. (2).

[17] R. J. C. Spreeuw, R. C. Neelen, N. J. van Druten, E. R. Eliel, and J. P. Woerdman, Phys. Rev. A **42**, 4315 (1990).

[18] R. J. C. Spreeuw, N. J. van Druten, M. W. Beijersbergen, E. R. Eliel, and J. P. Woerdman, Phys. Rev. Lett. **65**, 2642 (1990).

[19] The fit was obtained by fitting the frequency and linewidth data simultaneously, giving equal weight to each of the points.

[20] S. G. Johnson, M. Ibanescu, M. A. Skorobogatiy, O. Weisberg, J. D. Joannopoulos, and Y. Fink, Phys. Rev. E **65**, 066611 (2002).

[21] D. S. Kim, S. C. Hohng, V. Malyarchuk, Y. C. Yoon, Y. H. Ahn, K. J. Yee, J. W. Park, J. Kim, Q. H. Park, and C. Lienau, Phys. Rev. Lett. **91**, 143901 (2003).

Asymmetry reversal in the reflection from a two-dimensional photonic crystal

E. F. C. Driessen,* D. Stolwijk, and M. J. A. de Dood

Huygens Laboratory, Leiden University, P.O. Box 9504, 2300 RA Leiden, The Netherlands
*Corresponding author: driessen@molphys.leidenuniv.nl

The measured, angle-dependent, reflection spectra of a two-dimensional GaAs photonic crystal consist of an asymmetric peak on top of an oscillating background. At large angles of incidence (>70°), the asymmetry of the peak is observed to flip for *p*-polarized light. We explain the observed spectra with a Fano model that includes loss and interference between a resonant waveguide component and direct Fresnel reflection of the layered structure. We show that the reversal of the asymmetry of the line is due to a change in sign of the direct reflection at Brewster's angle. © 2007 Optical Society of America

OCIS codes: 230.3990, 230.7400, 230.5750, 050.2770.

Two-dimensional (2D) photonic crystal slabs have been studied widely, both theoretically and experimentally. These slabs contain a periodic arrangement of holes on a wavelength scale. Due to their structure they can prevent propagation of guided modes for a range of frequencies. The existence of this so-called bandgap and the related dispersion allow control of light on a wavelength scale [1].

Optical reflectivity measurements are a relatively easy way to characterize the properties of these slabs. The wavelength dependent spectra show a number of features related to leaky modes of the slab [2,3]. A lot of effort has been devoted to calculating these spectra by rigorously solving Maxwell's equations using scattering matrices [4,5], Green's functions [6], and finite difference time domain methods [2,7]. Although being able to reproduce the spectra, these calculations do not give physical insight into the origin of the spectral features. Therefore it is important to develop simpler models that can explain the measured resonances. Such models can be used as a diagnostic tool for fabricated structures and can facilitate the first design of a photonic crystal structure.

In this Letter, we present reflection measurements on a 2D photonic crystal slab. The asymmetry of the (Fano) lineshape [8,9] in the reflection spectra is observed to change as a function of angle of incidence. Our observations can be described with an extended coupled mode theory, linking the reversal of asymmetry to the change of sign of the Fresnel reflection coefficient of the layered structure. This change of sign occurs at Brewster's angle.

The photonic crystal in this study was fabricated in GaAs using e-beam lithography and reactive ion etching. It consists of a square lattice of 1000×1000 holes with radius $r \approx 100$ nm and lattice constant $a \approx 320$ nm. Figure 1 shows scanning electron microscope (SEM) images from the top (a) and a cross section (made with a focused ion beam) (b). Due to details of the fabrication process, the cross section of the holes consists of two slightly tapered parts, as can be seen in Fig. 1(b). The holes become wider until

a depth of ~600 nm and then narrow down until a depth of $1.5-2$ μm.

We measured the specular reflection from the photonic crystal along the Γ−X direction [indicated with the arrow in Fig. 1(a)] as a function of the angle of incidence from 25° to 80° in steps of 2.5°. White light from a spectrally broad lamp was polarized and focused onto the sample. The specular reflection was polarization-filtered, imaged onto a fiber, and analyzed in a spectrometer with a spectral resolution of ~2 nm. The numerical aperture (NA) of the incoming beam was limited to NA < 0.04. The spot size on the sample was ~100 μm. We measured the spectra for both polarizations, but show only the results for *p*-polarized light.

Reflection spectra for angles of incidence of 50, 70, and 80° are shown in Fig. 2. The spectra show a large, asymmetric peak on top of an oscillating background. By changing the angle of incidence, the peak shape in changes from asymmetric with a tail on the red side [Fig. 2(a)], to symmetric [Fig. 2(b)], to asymmetric with a tail on the blue side [Fig. 2(c)].

To explain our measurements, we extended the temporal coupled-mode theory in [9] by including an additional loss channel. Light incident onto the photonic crystal slab can be reflected through different channels: a nonresonant (direct), a resonant, and a
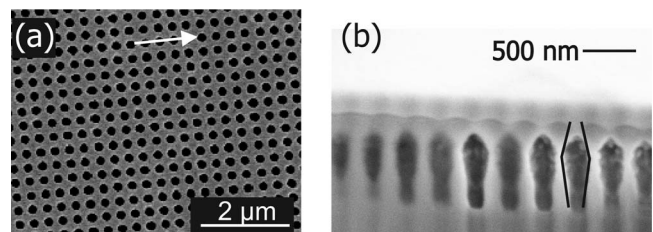

Fig. 1. (a) SEM image of the photonic crystal (top view) showing a square lattice of holes with a lattice constant of 320 nm and a diameter of ~100 nm. The arrow indicates the direction along which the reflectance is measured. (b) SEM image of the cross section of the photonic crystal slab (taken under an angle of 59°). The approximate shape of the holes is indicated with the black curves.
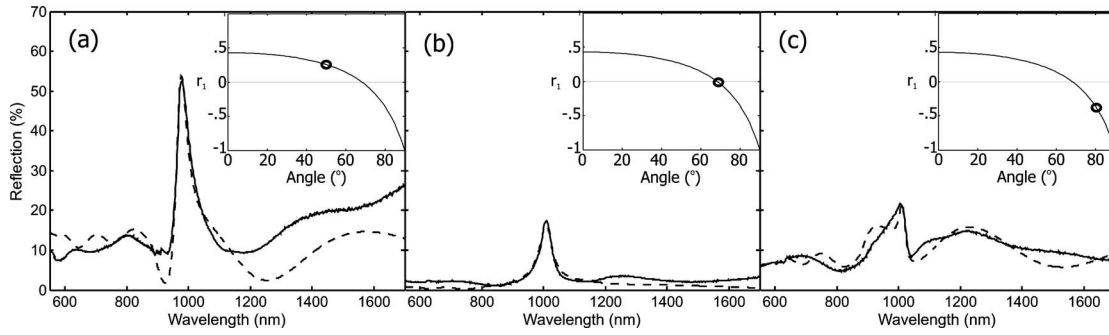
Fig. 2.   Experimental reflection spectra of the photonic crystal slab for three angles of incidence: (a) 50°, (b) 70°, and (c) 80°. The dashed curves are fits using the model discussed in the text. The insets show the reflection coefficient r_1 for an interface of air and $n_{\text{eff}}=2.5$, as a function of angle of incidence. The circles indicate the angle of the measurement.

loss channel. The direct channel corresponds to the Fresnel reflection of the layered system, while the resonant channel is created by coupling to a (leaky) waveguide mode. This waveguide mode has a well-defined dispersion relation and coupling at a specific frequency occurs via diffraction. The asymmetric Fano line shape can be explained by interference between the direct channel and the resonant channel. The additional loss channel allows to include the effects of scattering from surface roughness and diffraction into the substrate. All input and output channels of the system are linked by a direct-scattering matrix C and a resonant scattering matrix U. A vector $\mathbf{d}$ contains the (complex) coupling coefficients of the resonant mode to the three different channels.

The direct channel contains the reflection and transmission coefficients of the layered system. At each angle of incidence, we use Maxwell–Garnett's theory [10,11] to describe the photonic crystal layer as a birefringent layer with a refractive index n_{eff}. We then calculate the Fresnel reflection and transmission coefficients [12] of the layered system shown in Fig. 3(a), incorporating the known refractive index dispersion of GaAs [13], which includes absorption for wavelengths shorter than 950 nm. Taking the loss channel into account, we write the scattering matrix for the direct process as

$$C = \begin{bmatrix} r_1 & t & 0 \\ t & r_2 & 0 \\ 0 & 0 & 1 \end{bmatrix}, \qquad (1)$$

where r_1, r_2, and t are the (complex) Fresnel reflection and transmission coefficients for the electric field.

The resonant channel, due to the leaky waveguide, is formed by the photonic crystal layer. As pictured in Fig. 3(b), the incident light is partially diffracted into the waveguide and confined by internal reflection. The light that is diffracted back interferes with the directly reflected and transmitted light (channels 1 and 2 in Fig. 3). The resonance angular frequency ω_0 is determined by the dispersion relation of the waveguide mode involved. The average lifetime in the waveguide is parameterized by an escape time τ and is a function of angle of incidence. The scattering matrix describing the resonant channel is given by

$$U = \frac{\mathbf{d}\mathbf{d}^T}{i(\omega - \omega_0) + 1/\tau}, \qquad (2)$$

where ω is the angular frequency of the incident light.

In our experiment, the tapered form of the holes effectively ensures that there is a waveguide in the upper part of the photonic crystal layer. However, since the refractive index of the substrate is higher than the effective index of the photonic crystal layer, light propagating in the waveguide mode can still leak to the substrate without being diffracted. To incorporate these losses in the model, we added a third channel to the scattering matrix [channel 3 in Fig. 3(b)]. In this relatively simple model, we assume that a fraction Λ of the light is irreversibly lost in the resonant channel. This is valid as long as losses in the resonant channel are much larger than losses in the direct channel. This generally holds as long as the losses in the direct channel are small, since in this case the interaction length for light in the resonant channel is much larger than that in the direct channel. The effect of adding a loss channel is that the reflectivity no longer reaches 100% nor 0% as is the case for a system without loss [9].

Time-reversal symmetry and energy conservation put the following constraints on the coupling constants $\mathbf{d}$ [9]:

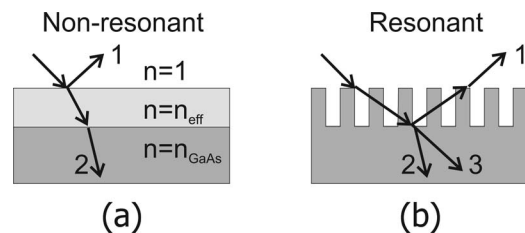$$C\mathbf{d}^* = -\mathbf{d}, \qquad (3)$$

Fig. 3.   Model for the (a) nonresonant and (b) resonant pathways in the model. The numbers indicate the different channels in the scattering matrix model. (a) Nonresonant pathways are modeled by applying effective medium theory to the photonic crystal layer and calculating the Fresnel reflection and transmission coefficients of the layered system. (b) For the resonant pathway, the incident light is refracted into a waveguide mode, which can diffract back to channels 1 and 2, but can also propagate into the substrate (3) leading to loss.

$$\mathbf{d}^{\dagger}\mathbf{d} = 2/\tau. \qquad (4)$$

Furthermore, the diffractive coupling to the resonant mode is assumed to be equally large on both sides of the photonic crystal slab (i.e., $|d_1|=|d_2|$). With these constraints, we can write the coupling constants $\mathbf{d}$ in terms of the Fresnel coefficients and the parameters ω_0, τ, and Λ. The reflectivity $R=|U_{11}+C_{11}|^2$ for the system is then given by

$$R = \left| \frac{i(\omega - \omega_0)r_1 + 1/\tau[\Lambda r_1 + (1-\Lambda)t]}{i(\omega - \omega_0) + 1/\tau} \right|^2. \qquad (5)$$

After setting the fill fraction and the thickness of the photonic crystal slab once, the Fresnel coefficients are fixed and there are only three free parameters left in the model: the resonance angular frequency ω_0, the resonance life time τ, and the leakage to the third channel Λ.

The dashed curves in Fig. 2 show the best fit of the model to our data. Although the fits deviate on detail from the measurements, qualitatively all elements of the measurements are contained in the model. We attribute most deviations from the measurements to simplifications we made with respect to the vertical shape of the air holes. Also, Maxwell–Garnett's effective medium theory is only valid when all relevant length scales in the system are much smaller than the wavelength, which is not true in our case.

Using the model described here, one can understand the origin of the change in asymmetry of peak shape when changing the angle of incidence. Since the peak is a product of interference between a resonant Lorentzian line and a nonresonant direct contribution, the relative phase between these two contributions will determine the asymmetry of the resulting line shape.

The Fresnel reflection coefficient for p-polarized light for a dielectric interface vanishes and changes sign at Brewster's angle. This is shown in the insets of Fig. 2, for an interface between air and a dielectric with $n_{\mathrm{eff}}=2.5$. It is exactly this change of sign that causes the line shape to vary from red-tailed asymmetric to Lorentzian at Brewster's angle to blue-tailed asymmetric for larger angles. For s-polarized light, we observed the line shape to be blue-tailed asymmetric for all angles of incidence, which confirms this explanation since the Fresnel reflection coefficient for s-polarized light is always negative.

The rough shape of the holes causes relatively broad spectral features that are easily resolved. The fact that we are able to describe our data with an extended version of a coupled mode theory and observe a change in asymmetry of the spectral line shows that the description is robust and also valid for less-than-perfect crystals.

In conclusion, the reflection spectra from a 2D photonic crystal show a large asymmetric peak on top of an oscillating background. With increasing angle of incidence, the asymmetry of the peak reverses. We explained all observations with an extended scattering matrix model [9] that includes additional loss. The reversal of the asymmetry is a consequence of the change in sign of the Fresnel reflection coefficient when crossing Brewster's angle. The presented model gives good qualitative as well as quantitative agreement with the measurements, while having only three fit parameters describing the resonance frequency and lifetime of the resonant waveguide mode, and its losses.

Although the model does not predict the position of the resonances for a given structure, these can be estimated for the case of a true waveguide (i.e., $n_{\mathrm{eff}} > n_{\mathrm{subs}}$, with n_{subs} the refractive index of the substrate) [14,15]. The model can easily be extended to incorporate multiple uncoupled waveguide modes, thus forming a powerful tool in explaining the observed phenomena in reflection spectra from 2D photonic crystals.

References

1. T. F. Krauss and R. M. De la Rue, Prog. Quantum Electron. **23**, 51 (1999).
2. M. Kanskar, P. Paddon, V. Pacradouni, R. Morin, A. Busch, J. F. Young, S. R. Johnson, J. MacKenzie, and T. Tiedje, Appl. Phys. Lett. **70**, 1438 (1997).
3. V. N. Astratov, D. M. Whittaker, I. S. Culshaw, R. M. Stevenson, M. S. Skolnick, T. F. Krauss, and R. M. De La Rue, Phys. Rev. B **60**, R16255 (1999).
4. L. Li, J. Opt. Soc. Am. A **14**, 2758 (1997).
5. D. M. Whittaker and I. S. Culshaw, Phys. Rev. B **60**, 2610 (1999).
6. A. R. Cowan, P. Paddon, V. Pacradouni, and J. F. Young, J. Opt. Soc. Am. A **18**, 1160 (2001).
7. S. Fan and J. D. Joannopoulos, Phys. Rev. B **65**, 235112 (2002).
8. U. Fano, Phys. Rev. **124**, 1866 (1961).
9. S. Fan, W. Suh, and J. D. Joannopoulos, J. Opt. Soc. Am. A **20**, 569 (2003).
10. J. C. Maxwell-Garnett, Philos. Trans. R. Soc. London **203**, 385 (1904).
11. J. C. Maxwell-Garnett, Philos. Trans. R. Soc. London **205**, 237 (1906).
12. M. Born and E. Wolf, *Principles of Optics*, 6th ed. (Pergamon, 1980).
13. E. D. Palik, *Handbook of Optical Constants of Solids* (Academic, 1985), Vol. 1.
14. L. C. Andreani and D. Gerace, Phys. Rev. B **73**, 235114 (2006).
15. D. Gao and Z. Zhou, Appl. Phys. Lett. **88**, 163105 (2006).

Index Matching of Surface Plasmons

D. Stolwijk[1], E.F.C. Driessen[1], M.A. Verschuuren[2], G.W. 't Hooft[1,2], M.P. van Exter[1], M.J.A. de Dood[1]

[1]Huygens Laboratory, Leiden University   [2]Photonic Materials and devices, Philips Research, Eindhoven

Introduction

The optical transmission through a metal nano-hole array is increased due to the excitation of surface plasmons. Most experimental structures are asymmetric and therefore the plasmons on different interfaces are not resonant. It is not clear what happens if a symmetric structure is created, such that the plasmons become resonant. To answer this question, we measured transmission spectra for gold arrays with a liquid or dielectric layer on the top side of the structure, and a hole array with glass pillars placed in each of the holes.

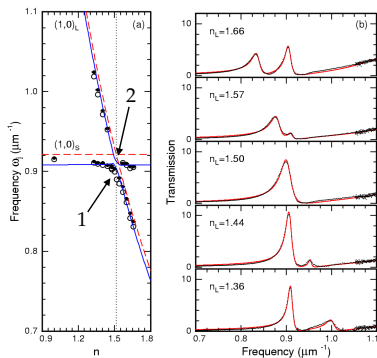## Typical Sample and Transmission Spectra

Imprinting Technique

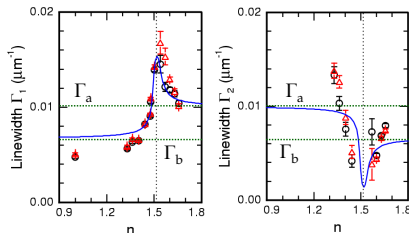
Remove gold from pillars

Remove pillars... or not
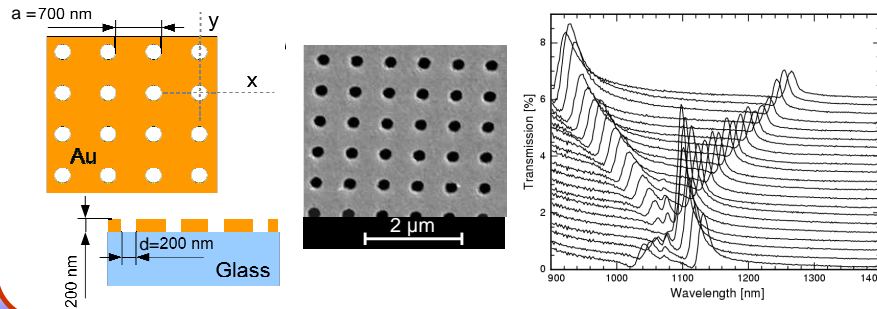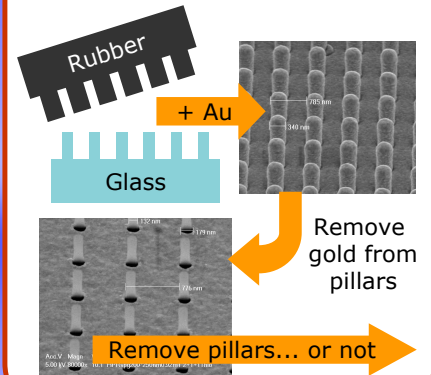
Liquid Index Matching

Square lattice, a = 700 nm, d = 200 nm

Fano type resonances cross as the refractive index is varied

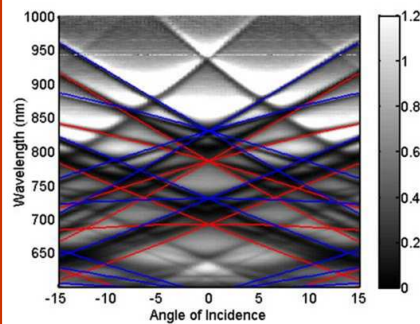Avoided crossing and observed linewidths prove coupling modes!

Coupled-mode theory:

$$i\frac{\mathrm{d}}{\mathrm{d}t}\begin{pmatrix} a \\ b \end{pmatrix} = H \begin{pmatrix} a \\ b \end{pmatrix} \quad \text{with}$$

$$H = \begin{pmatrix} \omega_a + V - i\Gamma_a & W + i\Gamma_C \\ W + i\Gamma_C & \omega_b + V - i\Gamma_b \end{pmatrix}.$$
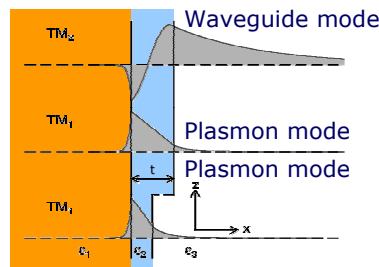
Off-diagonal elements describe conservative and dissipative coupling. Fit $\Gamma_a \neq \Gamma_b$ (roughness surface).

Solid Index Matching

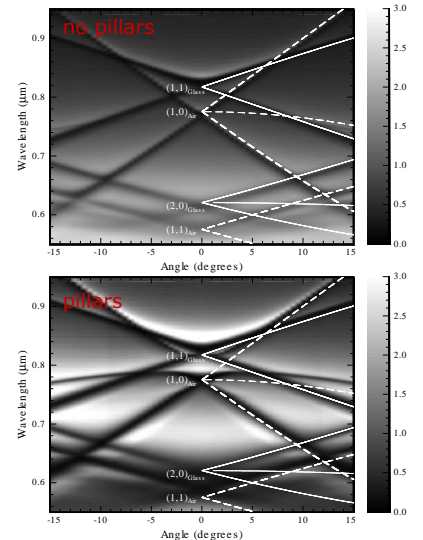Hexagonal lattice, a = 1060 nm, d = 135 nm, 340 nm SiO₂ layer

Thin layer of glass supports both surface plasmon modes and waveguide modes

Effect Pillars

Square lattice, a = 757 nm, d = 135 nm

Enhanced coupling to (0,±1)-modes: pillars act as antennas

Large (6%) splitting between modes

Conclusion and References

- Liquid index matching reveals coupling between plasmon modes
- A glass cover on top of the array shows waveguide modes
- Pillars enhance coupling to (0,±1)-modes and induce a large splitting

D. Stolwijk et al., "Enhanced Coupling of Surface Plasmons", accepted for Opt. Lett.

M.J.A. de Dood et al., "Observation of coupling between surface plasmons in index-matched hole arrays", submitted to Phys. Rev. B.